Check for updates

Tectonic evolution of the Northeastern Paleo-Tethys Ocean during the late Triassic: insights from depositional environment and provenance of the Xujiahe formation

Fenquan Xie[1], Wenzhou Xiao[2]*, Mabrouk Sami[3]*,
Ioan V. Sanislav[4], Mohamed S. Ahmed[5], Chenguang Zhang[6],
Yongkui Wang[7], Bingpeng Yan[7], Bing Hu[7], Ning Li[8] and
Douaa Fathy[9]

[1]Bohai-rim Energy Research Institute, Northeast Petroleum University, Qinhuangdao, China, [2]Hunan
Key Laboratory of Rare Metal Minerals Exploitation and Geological Disposal of Wastes, School of
Resource Environment and Safety Engineering, University of South China, Hengyang, China,
[3]Geosciences Department, College of Science, United Arab Emirates University, Al Ain, United Arab
Emirates, [4]Economic Geology Research Centre (EGRU), College of Science and Engineering, James
Cook University, Townsville, Australia, [5]Geology and Geophysics Department, College of Science,
King Saud University, Riyadh, Saudi Arabia, [6]School of Geographic Sciences, Xinyang Normal
University, Xinyang, China, [7]Shandong Provincial No.4 Institute of Geological and Mineral Survey,
Weifang, China, [8]Shandong Provincial No.1 Institute of Geological and Mineral Survey, Ji'nan, China,
[9]Geology Department, Faculty of Science, Minia University, El-Minia, Egypt

The Triassic tectonic evolution and affinity among the Yangtze Block, Qinling Orogenic Belt and Songpan-Ganzi Terrane remain subjects of ongoing scientific debate. In this context, the sedimentary rocks of Xujiahe Formation (second segment) (T_3x_2) represent an ideal case for addressing this issue. In this study, new stratigraphic, geochemical and detrital zircon analyses have been conducted on two sections of the T_3x_2. The stratigraphic assemblage and features suggests a braided delta as the depositional setting. Whole-rock geochemical results indicate that the sandstones from the T_3x_2 exhibit moderate palaeo-weathering and primarily originate from upper crustal felsic rocks, mostly S-type granites. The detrital zircons within these sandstones display distinctive age peaks at intervals of 200−300 Ma, 700−900 Ma, and 1800−2000 Ma, similar to those from the Qinling Orogenic Belt. Both the clastic particle composition and whole-rock geochemistry indicates that the T_3x_2 sections were deposited in a tectonic environment transitioning from a passive to an active continental margin, highlighted by a braided delta influenced by rivers flowing from the northeast to the southwest.

1 Introduction

The Xujiahe Formation, a late Triassic stratum, is widely distributed in the Sichuan Basin (Li et al., 2017; Jiang et al., 2023; Gou et al., 2024). As a stratum mainly composed of clastic rocks, the Xujiahe Formation is an ideal research object to constrain the provenance and tectonic evolution of the Sichuan Basin. Previous studies mainly located at the northwestern Sichuan Basin and considered that the Songpan-Ganzi Terrane and Longmenshan strike-slip fault zone provided the dominate detrital materials to the Xujiahe Formation (Yang et al., 2013; Li et al., 2014; Deng et al., 2019; Zhang et al., 2023b). However, many recent studies have proposed that the Qinling Orogenic Belt is the main origin of the detrital materials of the Xujiahe Formation (Luo et al., 2013; Mu et al., 2019; Jiang et al., 2023; Gou et al., 2024). Detrital materials transferred by a long ancient river from the Yangtze and Cathysia Blocks are also a viewpoint that provides a much more extensive detrital provenance (She, 2007; Yu and Liang, 2017). As a widespread stratum in the Sichuan Basin, the Xujiahe Formation has extensive detrital sources, which is reasonable. But the lack of systematic research on the Xujiahe Formation of the Northeastern Sichuan Basin led to an unclear understanding of the evolution of the Sichuan Basin and its affinity to the Northeastern Qinling Orogenic Belt. Furthermore, the controversy over the detrital provenance of the Xujiahe Formation caused different viewpoints on the tectonic evolution and affinity among the Yangtze Block, Qinling Orogenic Belt and Songpan-Ganzi Terrane (Li et al., 2014; Zhang et al., 2020; Gou et al., 2024).

As a super thick oil-gas reservoir layer, the T_3x_2 occupy the most percentage of the whole Xujiahe Formation (Huang et al., 2020; Liu et al., 2020; Yang et al., 2021; Liu et al., 2023; Cai et al., 2024). This segment is predominantly composed of clastic sediments, and it is an ideal representative of the whole Xujiahe Formation's provenance (Liao et al., 2010). In contrast, the other segments, primarily consisting of mudstone or shale, present challenges in provenance determination through geochemical methods due to their high loss on ignition and scarcity of detrital zircons (Deng et al., 2019; Zhou et al., 2019). This study focuses on samples from the second segment of the Xujiahe Formation. Comprehensive analyses, including whole-rock geochemistry of the sandstones, U-Pb isotopes and trace elements of detrital zircons, were conducted. These analyses aim to precisely determine the formation age of the Xujiahe Formation sedimentary rocks and identify their potential source rocks. This study provides new information for the Xujiahe Formation and the tectonic evolution of the Sichuan Basin.

2 Geological setting

The Sichuan Basin, located at the Northwestern corner of the Yangtze Block, is bordered by the Songpan-Ganzi Terrane to the Northwest and the Qinling Orogenic Belt to the North (Figure 1A). This region witnessed significant tectonic activity from the early to late Triassic, particularly the anticlockwise closure of the Paleo-Qinling Ocean along the eastern boundary of the Paleo-Tethys Ocean (Pullen et al., 2008; Gong et al., 2021), which led to the amalgamation of the Yangtze Block with the North China Craton. During this period, a substantial continental collision led first to the formation of the eastern Sulu-Dabie Orogenic Belt, followed by the formation of the western Qinling Orogenic Belt (Mu et al., 2019; Yuan et al., 2022; Li et al., 2023a). Subsequently, in the late Triassic, as the Paleo-Tethys Ocean continued to close, the Qiangtang Block began merging with the Yangtze Block and the Kunlun Orogenic Belt. This tectonic movement resulted in the creation of the Songpan-Ganzi Terrane and the Longmenshan strike-slip fault zone (Zhang et al., 2014).

The study area is situated in the Northeastern side of the Sichuan Basin, adjacent to the Songpan-Ganzi Terrane and Qinling Orogenic Belt (Figure 1B). The sedimentary strata of the study area extend continuously from Sinian to Quaternary. From Sinian to early Triassic, the sedimentary strata consist of passive continental margin basin sediments, featuring a mix of continental and shallow-sea facies rocks. While, from late Triassic to Tertiary, the sedimentary strata are predominantly foreland basin sediments, mainly comprising terrigenous clastic rocks. The study area is characterized by extremely thick sedimentary rock layers and a scarcity of exposed igneous rocks. Furthermore, the deep fractures in the study area exhibit two primary orientations: near the Longmenshan strike-slip fault zone on the west, the deep faults predominantly follow a NE-SW-direction, while near the Qinling Orogenic Belt on the east, the deep faults are mainly NW-SE-trending.
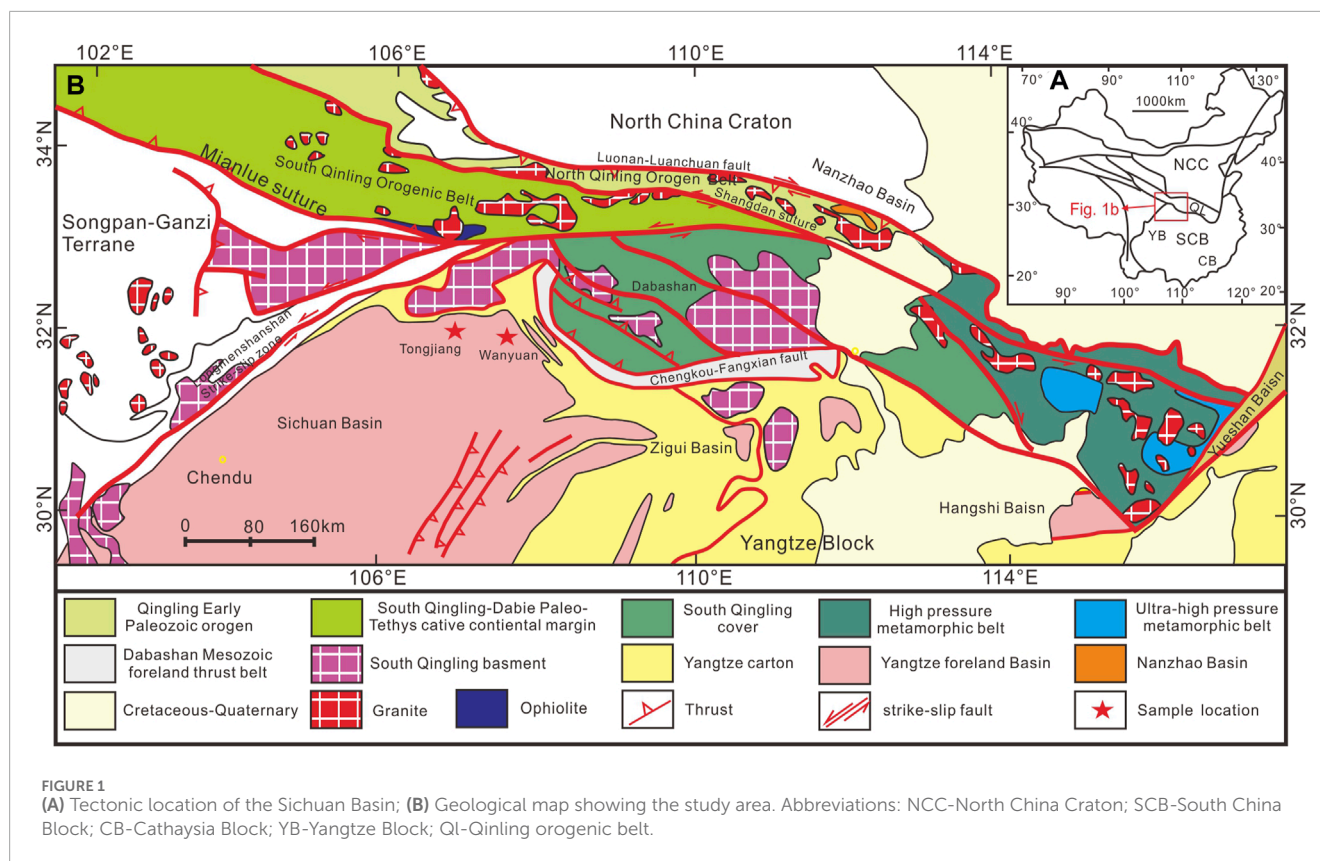
2.1 Songpan-Ganzi Terrane and Longmenshan strike-slip fault zone

The Songpan-Ganzi Terrane, as a flysch zone, represents the accretionary wedge associated with the subduction of the Paleo-Tethys Ocean (Gong et al., 2021). This terrane is predominantly covered by thick Triassic flysch sediments. During the late Triassic to Jurassic, the Songpan-Ganzi terrane experienced continuous deformation and uplift, accompanied by large-scale magmatic events led to the formation of felsic plutons of calc-alkaline, alkaline, peralkaline and peraluminous series granitic rocks (Yan et al., 2018b; Chen et al., 2023).

The NE-striking Longmenshan strike-slip fault zone extends ~500 km from southwest to the Northeast, which is composed of a Precambrian basement overlaid with Paleozoic (Cambrian to Permian) strata (Yan et al., 2018a). Since the late Triassic, the Longmenshan strike-slip fault zone has experienced three distinct tectonic deformation stages: a late Triassic compressional deformation, a Jurassic extensional deformation and a Quaternary stage marked by thrust, strike-slip fault zone and uplift tectonics (Yan et al., 2018b).

2.2 Qinling Orogenic Belt

The Qinling Oogenic Belt is divided into two distinct terranes: the North Qinling and South Qinling Blocks. These blocks were formed through the subduction of the Paleo-Qinling Ocean, a part of the Paleo-Tethys Ocean, and later ultimately amalgamated along the Shangdan suture zone, joining with the Yangtze Block and the

FIGURE 1
(A) Tectonic location of the Sichuan Basin; **(B)** Geological map showing the study area. Abbreviations: NCC-North China Craton; SCB-South China Block; CB-Cathaysia Block; YB-Yangtze Block; Ql-Qinling orogenic belt.

North China Craton (Han et al., 2024). The South Qinling Block, which is adjacent to the study area, is composed of a Precambrian basement covered by Sinian to Triassic sedimentary strata. Since the late Triassic, this block experienced intense magmatic events, evidenced by the discovery of large-scale syn-collisional Triassic S-type granites and post-collisional Jurassic I- and A-type granites (Tang et al., 2023; Xu, 2023). The North Qinling Block is composed of a Proterozoic basement overlaid with Paleozoic sedimentary strata, extensively intruded by Paleozoic magmatic rocks (Hao et al., 2024).

2.3 Yangtze Block

The Yangtze Block is regarded as an independent craton due to the discovery of its Archean basement (Qiu et al., 2018). This Block constitutes the Northwestern part of the South China Block and amalgamated with the Cathaysia Block along the Jiangnan orogenic belt during the Neoproterozic (Zhang and Zheng, 2013). Its geological features comprise an Archean basement overlain by Neoproterozoic to Cenozoic sedimentary strata. The Neoproterozoic to Triassic strata are mainly marine facies sediments, interlayered with middle-late Permian Emeishan lava. The Triassic to Cenozoic strata consists mainly of terrigenous clastic rocks. The igneous rocks within the Yangtze Block are notable for their isotopic ages, which predominantly fall within the Archean, Neoproterozoic, and Permian (Charvest, 2013).

3 Stratigraphy and sampling

3.1 Xujiahe formation

The Xujiahe Formation, known as a coal measure formation, is a late Triassic stratum composed of conglomerate, sandstone and mudstone, and is rich in plants and shellfish fossils. This formation was divided into six segments due to different sedimentary environment. The first segment is composed of fine sandstones, silty mudstones and carbon mudstones with thin interlayers of coal. The second segment, the primary focus of this study, is characterized by thick layers of medium to coarse sandstones underline with conglomerates. The third segment comprises shale and silty mudstones with coal interlayers. The fourth segment composed mainly of boulder conglomerates, pebbly coarse sandstones and coarse sandstones. The fifth segment is composed of siltstones, silty mudstones and carbon mudstones. The sixth segment is mainly made up of medium to coarse sandstones. Notably, the second and fourth segments are the main oil-gas reservoirs among the whole Xujiahe Formation, with the second segment being the thickest. This study involved petrographic and geochemical analysis of samples from the second segment of the Xujiahe Formation, collected from two sections in the Northeastern Sichuan Basin: the Wanyuan Shiguansi section (WSS) and the Tongjiang Nuoshuihetang Erpingcun section (TNES). These samples were collected for detailed petrographic and geochemical studies, including whole-rock geochemical analysis and zircon U-Pb dating (Table 1; Figure 2).

TABLE 1 Collected samples from WSS and TNES of Xujiahe formation.

Section	Sample for microscopic observation	Sample for clastic particle composition statistics	Sample for whole-rock geochemical study	Sample for zircon U–Pb dating
WSS	Wyb1	Wyb1	WYH1	WYG1
		Wyb2	WYH2	
	Wyb3	Wyb3	WYH3	WYG3
		Wyb4	WYH4	
TNES		Tjb1	TJH1	TJG1
	Tjb2	Tjb2	TJH2	
	Tjb3	Tjb3	TJH3	TJG3
			TJH3c	

3.2 Wanyuan Shiguansi section

The Wanyuan Shiguansi section (WSS; 108°01′36.84″E–32°02′24.31″N), is lies on the flank of an anticline. The core of the anticline is composed of the underlying Leikoupo group strata which exposed as pelitic strip dolomites. Notably, the first segment of the Xujiahe Formation is absent in this section. However, the upper Xujiahe Formation, specifically the second segment, displays a parallel unconformity with the underlying Leikoupo group (Figure 2).

In this section, the T_3x_2 exhibits a thickness of approximately 80 m. The lithological composition includes, from bottom to top, conglomerate-bearing coarse sandstone, medium-grained lithic quartz sandstone and fine-grained lithic quartz sandstone (Figures 3A,B). Four samples are collected from different layers. Samples are medium and fine-grained lithic quartz sandstones, with poor to medium sorting and roundness, and with grain sizes ranging from of 0.1–0.5 mm. Under the microscope, samples are composed of quartz (65–70%), feldspar (~5%), lithic fragment (~20%) and interstitial material (5–10%). The quartz predominantly appears as single-crystal quartz, the feldspar is mainly K-feldspar with minor microcline, and the lithic fragments are mainly siltstone and slate. The interstitial materials are primarily silty and argillaceous, supplemented by a small amount of carbonate minerals (Figures 3E,F).

3.3 Tongjiang Nuoshuihetang Erpingcun section

The Tongjiang Nuoshuihetang Erpingcun section (TNES; 107°10′44.79″E–32°22′09.3″N), comprises strata from the underlying Leikoupo group and overlying first and second segments of the Xujiahe Formation. The Leikoupo group is a middle Triassic strata and exposed mainly as pelitic strip dolomites and calcite dolomites. The first segment

of the Xujiahe Formation, forming the upper layer, is exposed as mudstones with interlayers of fine sandstones and silty mudstones. However, due to extensive coverage, the boundary between the Leikoupo group and the first segment of the Xujiahe Formation cannot be observed (Figure 2).

The T_3x_2 exhibits a clear boundary with the first segment. It has a total thickness of 170 m, and can be divided into two parts. The middle-lower part (0–110 m) features, from bottom to top, a lithological sequence of mudstone, siltstone, conglomerate and sandstone. The upper part (110–170 m) comprises silty mudstone, argillaceous siltstone and medium-coarse sandstone. Three samples are collected from different layers of the middle and lower part (Figure 2). These samples are medium-grained lithic quartz sandstones, characterized by poor sorting, medium roundness, and grain sizes of 0.1–0.5 mm (Figures 3C, D). Microscopic examination reveals a composition of quartz (~70%), feldspar (~5%), lithic fragment (15–20%) and interstitial material (5–10%). The quartz is predominantly single-crystal, the feldspar is chiefly K-feldspar with some microcline, and the lithic fragments mainly comprise siltstone, andesite, schist, and phyllite. Interstitial materials are largely silty and argillaceous, accompanied by a small amount of carbonate minerals (Figures 3G, H).

4 Analytical methods

4.1 Whole-rock major and trace element analysis

The analysis of the major and trace elements in the whole-rock samples was conducted at ALS Chemex in Guangzhou, China. The preparation of these samples involved pulverizing them in a crusher until they were fine enough to pass through a 200 mesh. The major element content was determined using a Panalytical
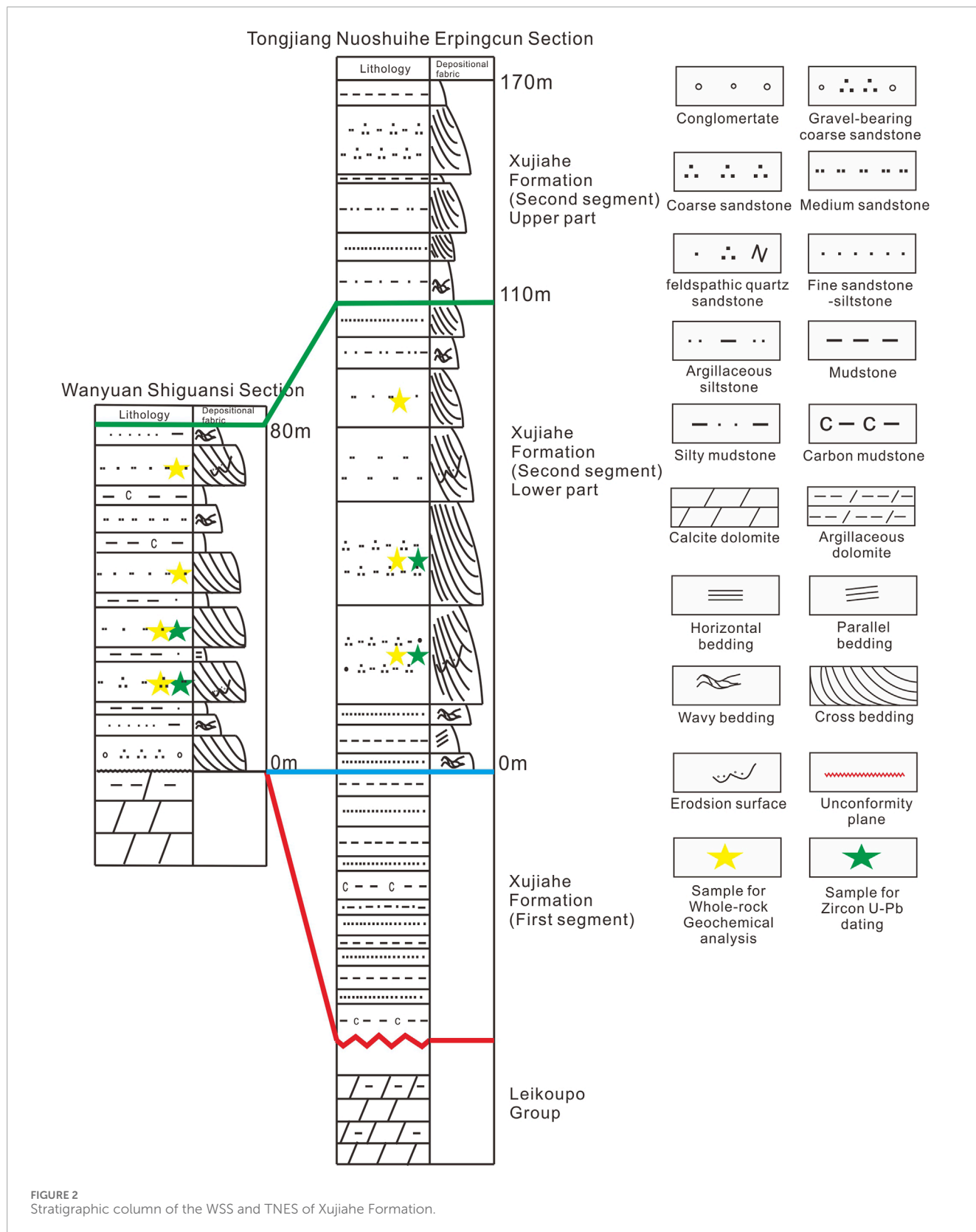
FIGURE 2
Stratigraphic column of the WSS and TNES of Xujiahe Formation.

Axios Max X-ray fluorescence (XRF) instrument, achieving an analytical accuracy ranging from 1% to 5%. For trace element analysis, an ICP-MS instrument (Perkin Elmer Elan 9,000) was employed, offering an analytical accuracy of better than 5%. More details about the analytical methods are provided by Qiu et al. (2017) and Zhang et al. (2018).
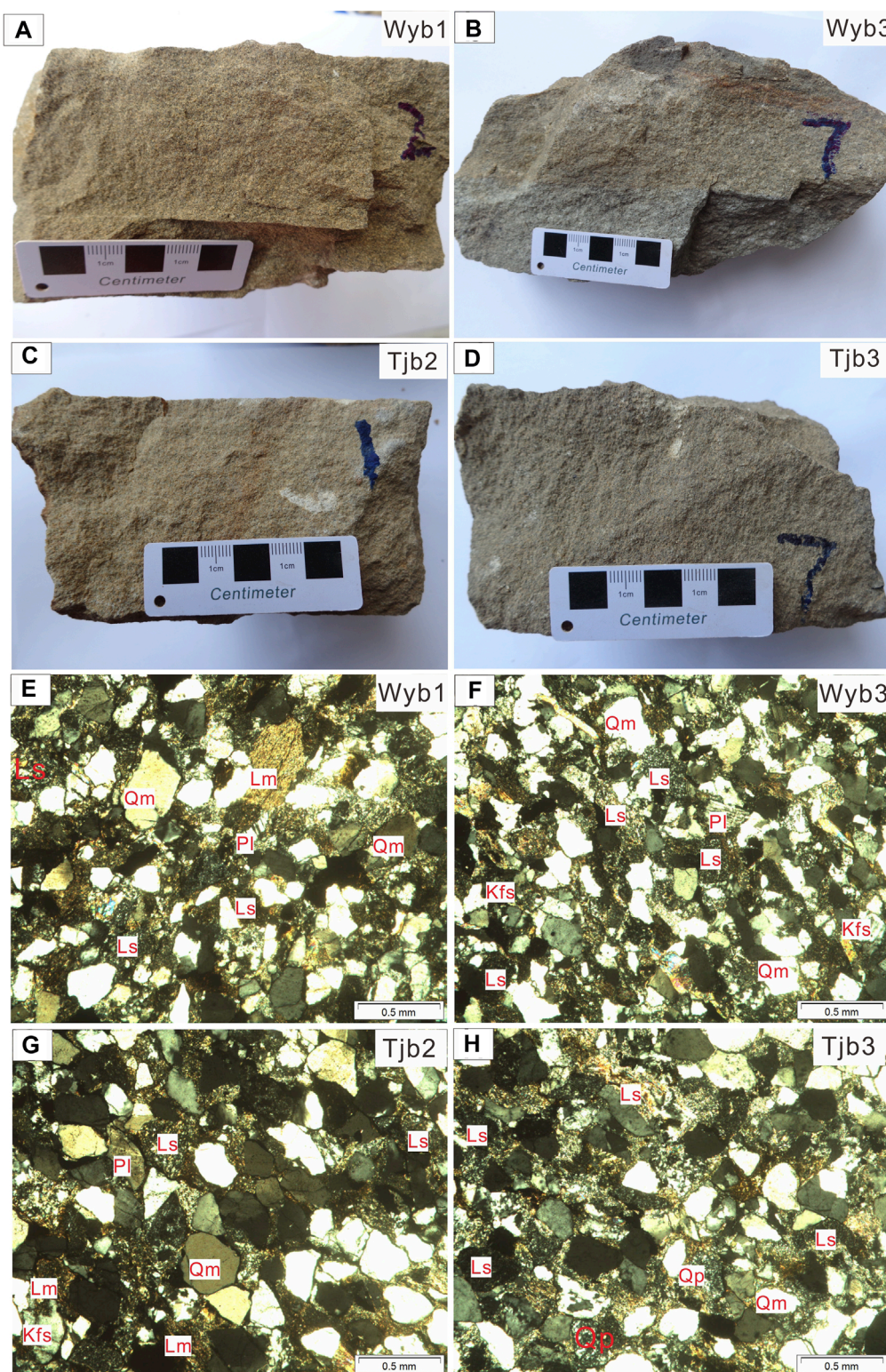
FIGURE 3
(A–D) Hand specimen and **(E–H)** microscopic photos of sandstone samples from the WSS and TNES. Abbreviations: Qm-monocrystalline quartz; Qp-polycrystalline quartz; Pl-plagioclase; Kfs-K-feldspar; Ls-lithic fragments of sedimentary rocks; Lm-lithic fragments of metamorphic rocks; Lv-lithic fragments of volcanic rocks.

4.2 Detrital zircon geochronology and trace elements composition

The separation of zircon grains was carried out using standard magnetic and heavy liquid methods at Langfang Integrity Geological Services Co., Ltd. These grains were then meticulously selected under a binocular microscope. To minimize any risk of contamination, the mineral separation laboratory maintains a clean environment, rigorously excluding dust. After each use, the pulverizer and ore beneficiation equipment were thoroughly washed with water and then air-dried for 15–30 min to eliminate any residual particles. The zircon grains were subsequently embedded in epoxy resin blocks and polished to achieve flat surfaces. For visualizing the internal structure of the zircon grains, Cathodoluminescence (CL) imaging was performed using a scanning electron microscope (SEM) at Chongqing Yujing Science and Technology Services Co. Ltd.

U-Pb geochronology and trace element analyses of zircon were conducted using laser ablation inductively coupled plasma-mass spectrometry (LA-ICP-MS) at Nanjing FocuMS Technology Co., Ltd. The setup included a Teledyne Cetac Technologies Analyte Excite LA system from Bozeman, Montana, USA, and an Agilent Technologies 7,700× quadrupole ICP-MS from Hachioji, Tokyo, Japan. The 193-nm ArF excimer laser, which was homogenized by a set of beam delivery systems, was focused on the zircon surface with a fluence of 6.0 J cm^{-2}. The ablation process involved a 35 μm spot diameter, at an 8 Hz repetition rate for 40 s, totaling 320 pulses. Helium was employed as the carrier gas to transport the aerosol efficiently to the ICP-MS. Zircon 91,500 served as the external standard for correcting instrumental mass discrimination and elemental fractionation, while Zircon GJ-1 was used for quality control in geochronology. The calibration of lead and other trace elements in zircon was externally performed against NIST SRM 610, with Si as the internal standard, following the methodologies of Liu Y. et al. (2010) and Hu et al. (2011). Raw data reductions were performed offline using ICPMSDataCal software (Liu et al., 2010a; b), quantitative calibration for Pb isotope dating was performed by ComPbcorr#3_18 (Andersen, 2002), and Concordia diagrams and weighted mean calculations were performed using ISOPLOT 4.15 (Ludwig, 2003).

4.3 Clastic particle composition statistics

The composition of clastic particles in the collected samples was analyzed using the Gazzi-Dickinson method (Ingersoll et al., 1984). This method involves drawing three straight lines across the thin section of the rock and counting the number of quartz, feldspar, and lithic fragments with a particle size between 0.2 and 2 mm that intersect these lines from left to right. To ensure accuracy and statistical significance, about 500 particles were counted per sample. Samples with a high concentration of carbonate or those comprising more than a quarter of impurities and cements were excluded from the count. However, particles affected by metasomatism were included in the count, based on their remaining clastic components.

5 Results

5.1 Whole-rock major and trace elements

Eight samples, four each from the WSS and TNES, were chosen for comprehensive whole-rock geochemical analysis, the results are present in Supplementary Table S1. The WSS samples exhibit high concentration of SiO_2 (66.95–80.63 wt%) and Al_2O_3 (9.51–10.40 wt%), with low content of MgO (0.97–2.49 wt%) and Fe_2O_3 (2.54–3.30 wt%). Their CaO (0.20–5.35 wt%), Na_2O (0.30–1.73 wt%) and K_2O (1.79–2.62 wt%) contents are moderate. Similarly, the TNES samples show high SiO_2 (66.95–80.63 wt%) and Al_2O_3 (9.51–10.40 wt%) contents, but lower MgO (0.41–0.51 wt%) and Fe_2O_3 (1.38–3.32 wt%) concentrations, and moderate CaO (0.05–0.17 wt%), Na_2O (0.03–0.09 wt%) and K_2O (1.69–2.20 wt%) composition. On the $log(SiO_2/Al_2O_3)$–$log (Na_2O/K_2O)$ diagram, the WSS samples predominantly fall within the litharenite and subarkose fields, whereas the TNES samples are chiefly in the arkose field. The $log(SiO_2/Al_2O_3)$–$log (Fe_2O_3/K_2O)$ diagram further illustrates that the WSS samples mainly align with the litharenite field, while the TNES samples align with the arkose field (Figures 4A,B).

Samples from the WSS and TNES have similar trace element distribution patterns both in primitive mantle and upper crust normalized diagrams, they show enrichment in P and depletion in Ba, Sr and Ti (Figures 4D,F). Additionally, they are characterized by a high concentration of rare earth elements (REEs), with a particular enrichment in light REEs compared to heavy REEs when normalized to C1 chondrite. The REE distribution patterns typically show a right-dipping shape in chondrite normalized diagram, coupled with slight negative Eu anomalies (Figure 4C). However, they show a relatively flat shape in upper crust normalized diagram, without Eu anomalies (Figure 4E).

5.2 Zircon U-Pb ages

A pair of samples from both the WSS and the TNES were selected for zircon U-Pb dating. The dating results are present in Supplementary Table S2 and their CL images and age distributions are shown in Figure 5.

In the analysis of sample WYG2 from the WSS, 70 zircons were randomly chosen for U-Pb isotopic analyses. Among these, 69 yielded consistent and concordant data. The determined ages of these zircons vary widely, ranging between 210 and 2,672 Ma. Notably, five distinct age peaks are evident at 200–300 Ma, 400–600 Ma, 700–900 Ma, 1800–2000 Ma, and 2,500 Ma (Figures 6A, B).

From sample WYG3 of the WSS, a set of 70 zircons were randomly chosen for U-Pb isotopic analysis. Among these, 66 zircons provided concordant results. The age range of these zircons extends from 276 to 3,290 Ma, with prominent age peaks primarily occurring at 200–300 Ma, 700–900 Ma, 1800–2000 Ma, and 2,500 Ma (Figures 6C,D).

In the case of sample TJG1 from the TNES, a total of 70 zircons were selected at random to undergo U-Pb isotopic analyses.
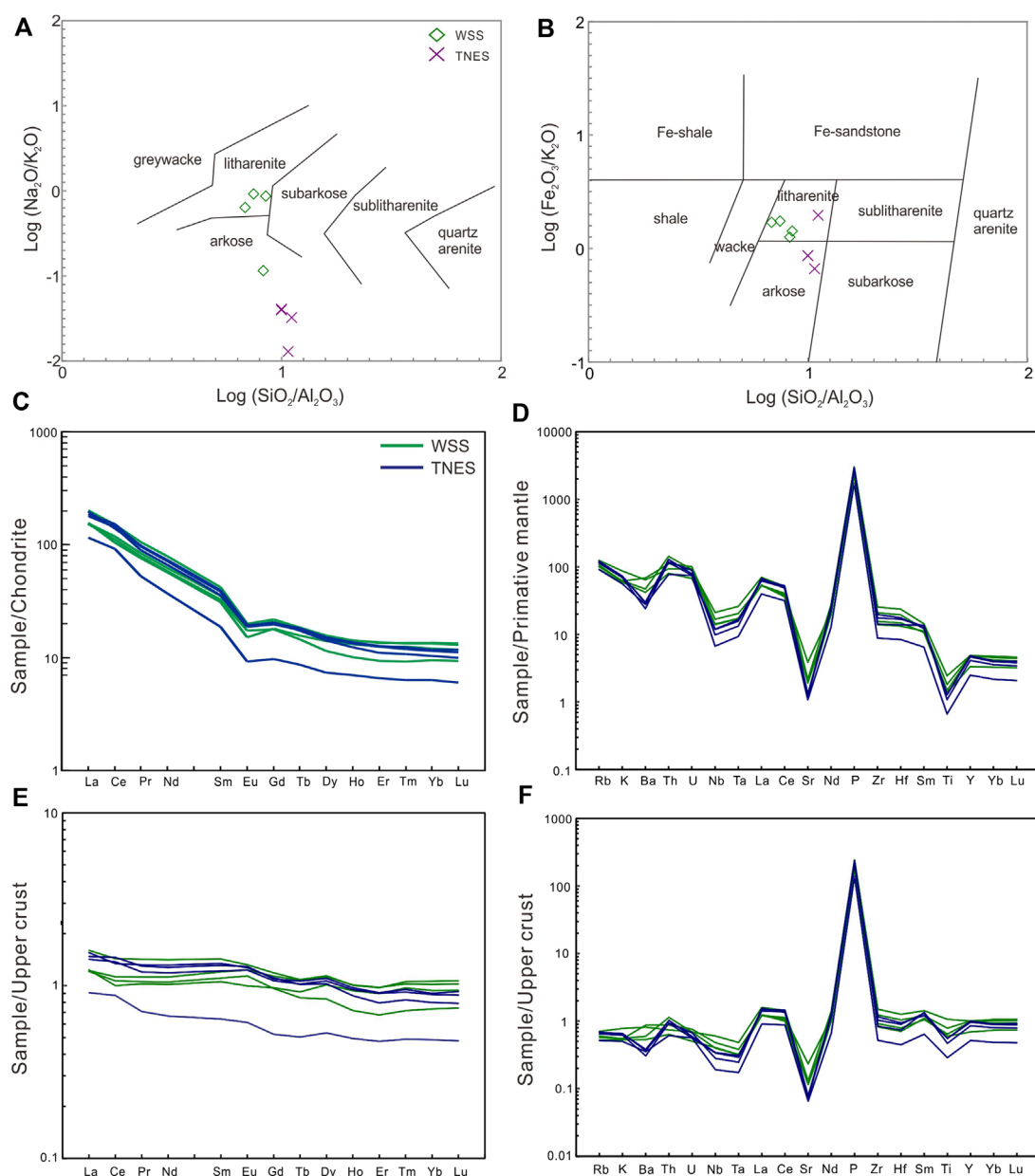
FIGURE 4
(A) log(Na$_2$O/K$_2$O)−log(SiO$_2$/Al$_2$O$_3$) diagram (after Pettijohn et al., 1972); **(B)** log(Fe$_2$O$_3$/K$_2$O)−log(SiO$_2$/Al$_2$O$_3$) diagram (after Herron, 1988); **(C)** Chondrite-normalized rare earth element distribution pattern diagrams of sandstone samples; **(D)** Primitive mantle-normalized trace element spider diagrams; **(E)** Upper crust-normalized rare earth element distribution pattern diagrams of sandstone samples; **(F)** Upper crust -normalized trace element spider diagrams. Normalizations are taken after Taylor and McLennan (1985) and Sun and McDonough (1989).

From this selection, 61 zircons yielded consistent and reliable data. The age range for these zircons spans from 219 to 2,599 Ma, with the most pronounced age peaks occurring at 200–300 Ma and 1800–2000 Ma (Figures 6E,F).

For sample TJG3 of the TNES, 70 zircons were randomly selected for U-Pb isotopic analyses. Of this group, 59 zircons yielded concordant data. These zircons exhibit a wide age range, spanning from 223 to 2,611 Ma, and are primarily characterized by two significant age peaks at the intervals of 200–300 Ma and 1800–2000 Ma (Figures 6G,H).

5.3 Zircon trace elements

Detailed analytical data for zircon trace elements are provided in Supplementary Table S3. In samples WYG2, WYG3, TJG1 and TJG3, most zircons exhibit low LREEs and high HREEs concentrations. They also exhibit significant positive Ce and negative Eu anomalies. This REEs pattern closely mirrors that found in magmatic zircons, although a small subset exhibit shows La concentrations below the detection limit. Some zircons show high LREE contents with slight positive Ce anomalies, which is similar to
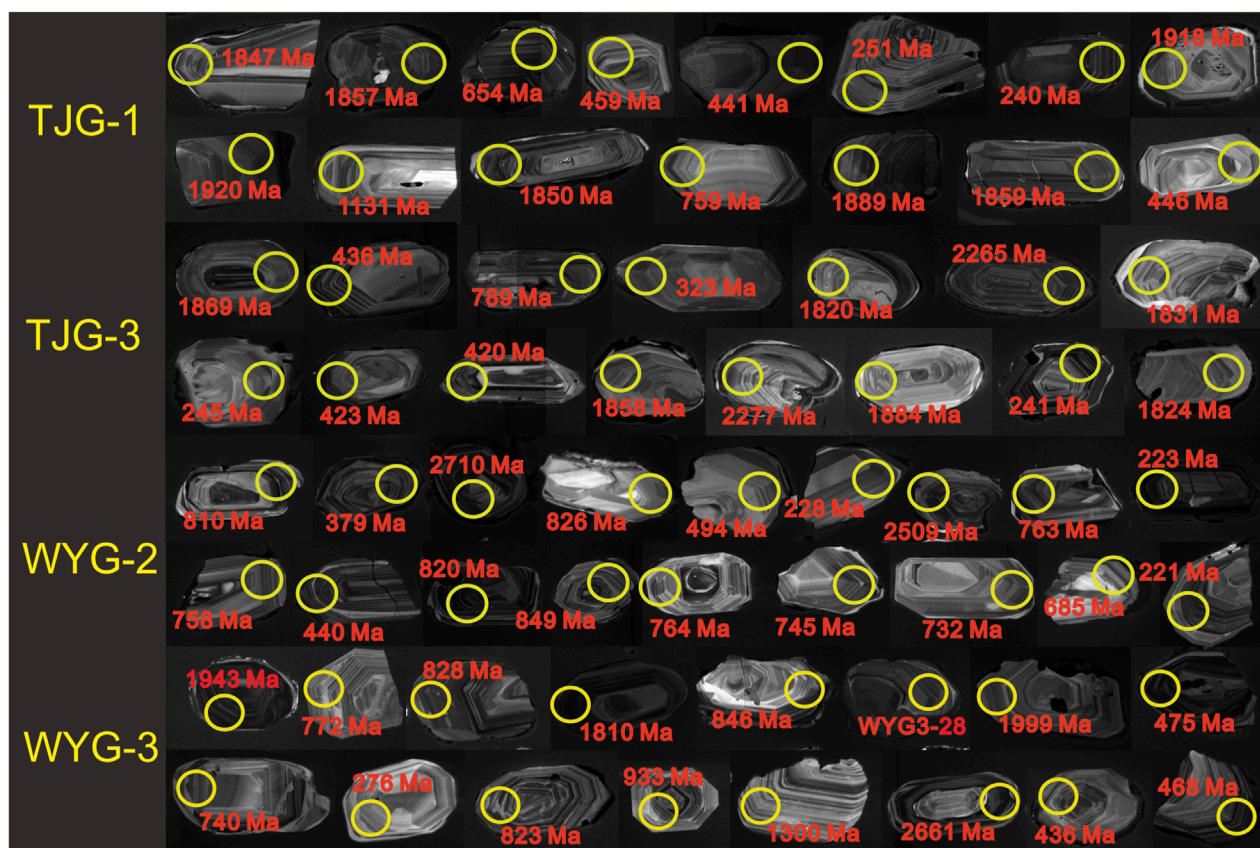
FIGURE 5
Representative zircon CL images from the WSS and TNES.

the REE distribution pattern of hydrothermal zircons or some types of metamorphic zircons (Figure 7).

For zircons in sample WYG2, the Th/U ratios range from 0.05 to 2.03. Out of 140 analyzed grains, 124 exhibit Th/U ratios greater than 0.3, 12 have ratios between 0.1 and 0.3, and 4 possess ratios less than 0.1. Similarly, zircons from sample WYG3 display Th/U ratios within the same range of 0.05–2.03, with an identical distribution among the 140 grains. The same Th/U ratio pattern is observed in samples TJG1 and TJG3: in each of these samples, out of 140 grains, 124 have Th/U ratios over 0.3, 12 grains range between 0.1 and 0.3, and 4 are below 0.1 (Figure 8).

5.4 Clastic particle composition

The statistics results of clastic particle composition are provided in Supplementary Table S4. The samples from the WSS are characterized by a high proportion of quartz (27.2%–59.2%), low propotion of feldspars (5.1%–12.0%) and lithic fragments (28.4%–45.2%). Among these lithic fragments in the WSS samples, sedimentary fragments represent the highest proportion at 51%, metamorphic fragments come next with 27%, and volcanic fragments are the least with 22%.

In the samples from the TNES, a significant proportion of quartz (27.2%–59.2%) is noted. These samples also exhibit a lower proportion of feldspars (5.1%–12.0%) and lithic fragments (28.4%–45.2%). Within the lithic fragment component, sediment fragments are the most prominent (44%), followed by volcanic fragments at a moderate level of 32%, and the least proportion is the metamorphic fragments (24%).

6 Discussion

6.1 Depositional environment and ages

The T_3x_2 is divided into two sections: the middle-lower part, corresponding to its early formation, and the upper part, indicative of its later formation. In the WSS, due to erosion, only the middle-lower part is present at the topmost layer. In both the WSS and the TNES, the sandstone of the middle-lower part typically features an incomplete erosion surface with gravel. Progressing from the bottom upwards, there is a gradual decrease in gravel proportion and a corresponding reduction in sandstone grain size. The sandstone layers exhibit a pattern of alternating parallel and cross bedding. The parallel bedding is formed under a strong hydrodynamic environment, with the sediments delaminated from coarse-to fine-grained during their migration due to their density. In contrast, cross bedding is typical of environments with braided distributary
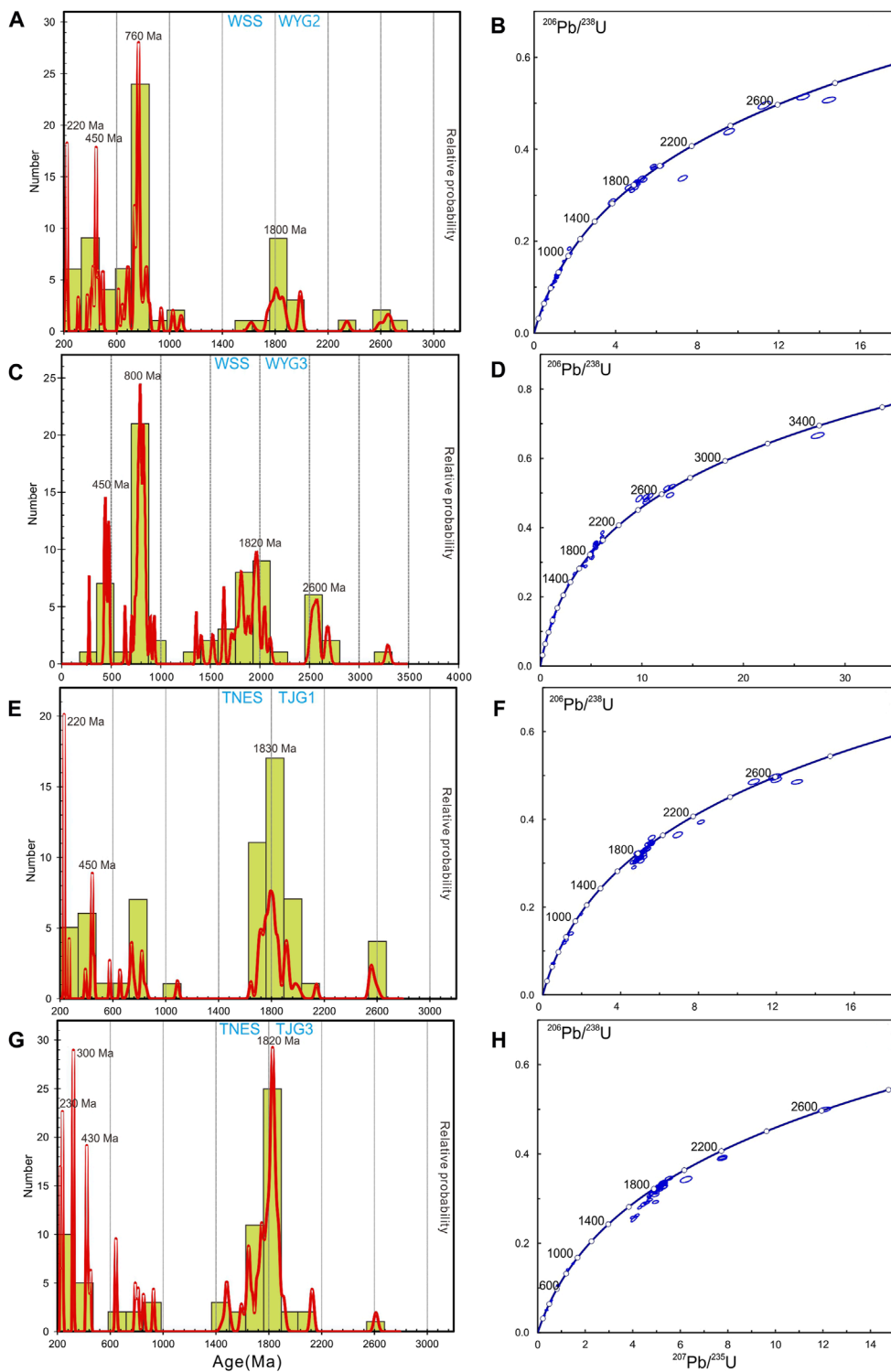
FIGURE 6
(A,C,E and G) Detrital zircon age distributions with significant peak ages and **(B,D,F and H)** U–Pb Concordia diagrams of sandstone samples from the WSS and TNES.

channels that periodically alter their course and flow direction. These observations suggest that the middle-lower part of the T_3x_2 in the WSS and TNES was likely deposited in a braided delta plain facies.

Compared to the lower layers, the upper part of the T_3x_2 predominantly features sandstone with convolute bedding and slump deposits. These characteristics suggest a subfluvial, rapid depositional environment marked by turbulent flow. Additionally,
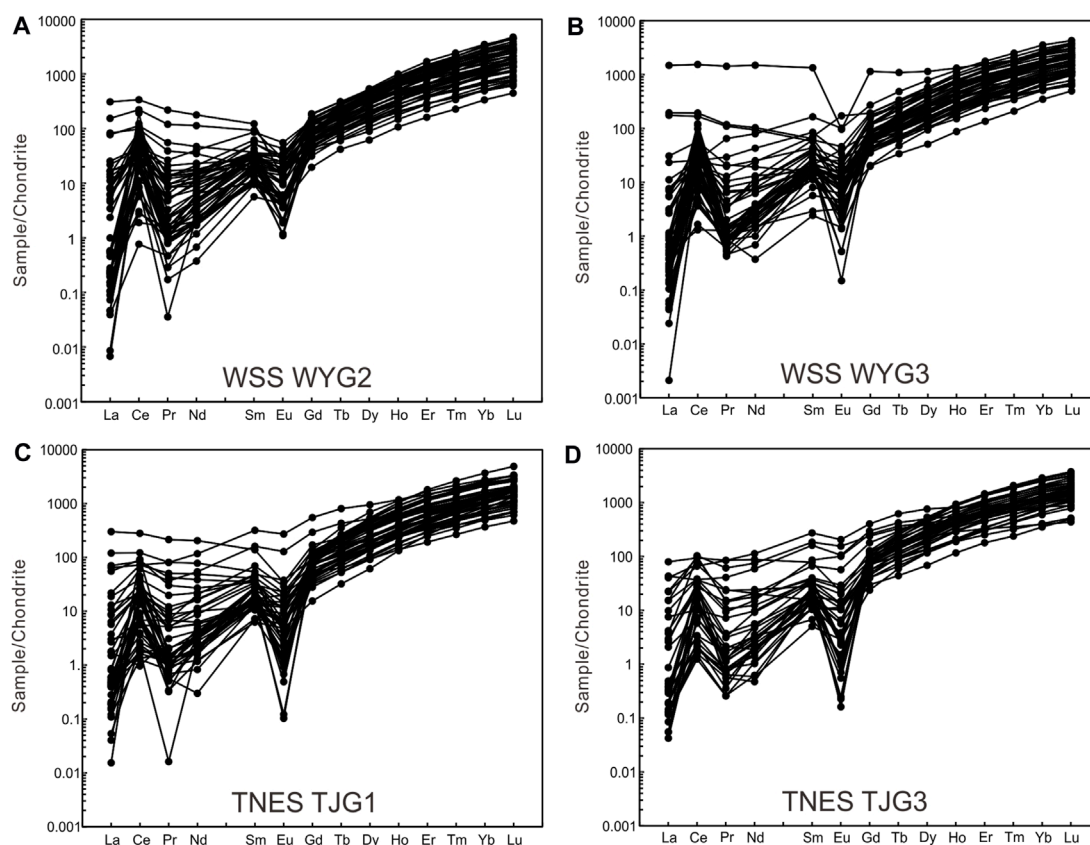
FIGURE 7
Chondrite-normalized rare earth element distribution pattern diagrams of detrital zircons from the WSS and TNES. The Chondrite-normalized and primitive mantle-normalized values are from Sun and McDonough (1989).
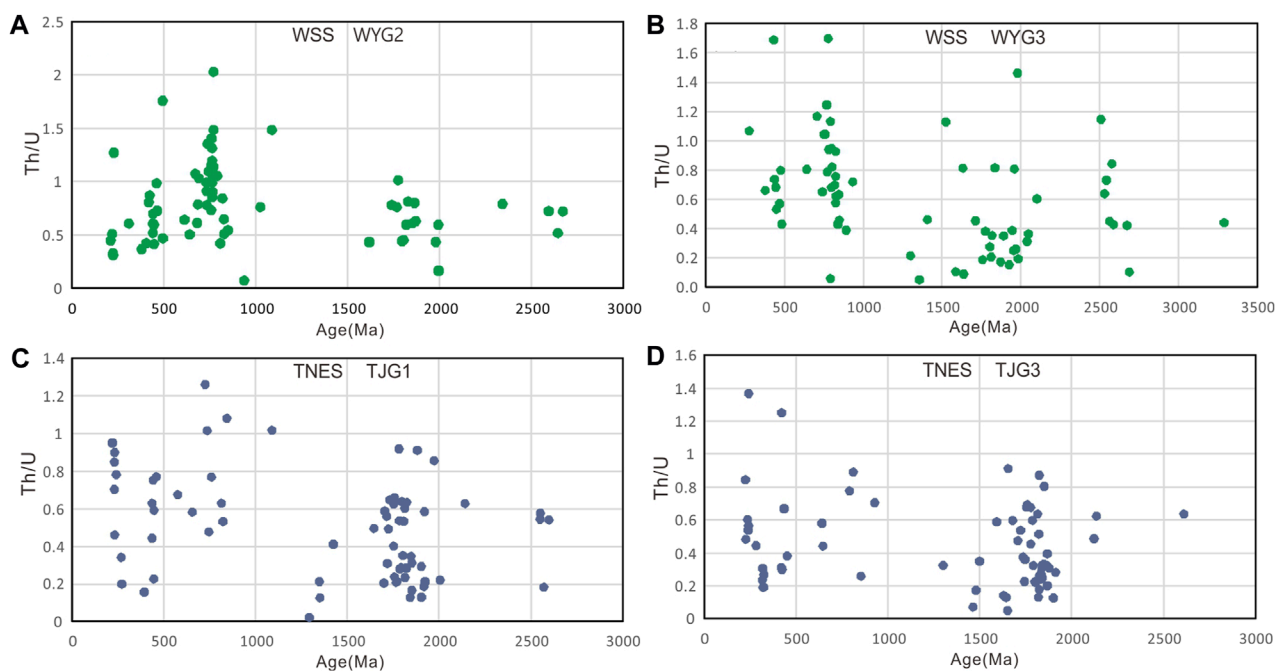

FIGURE 8
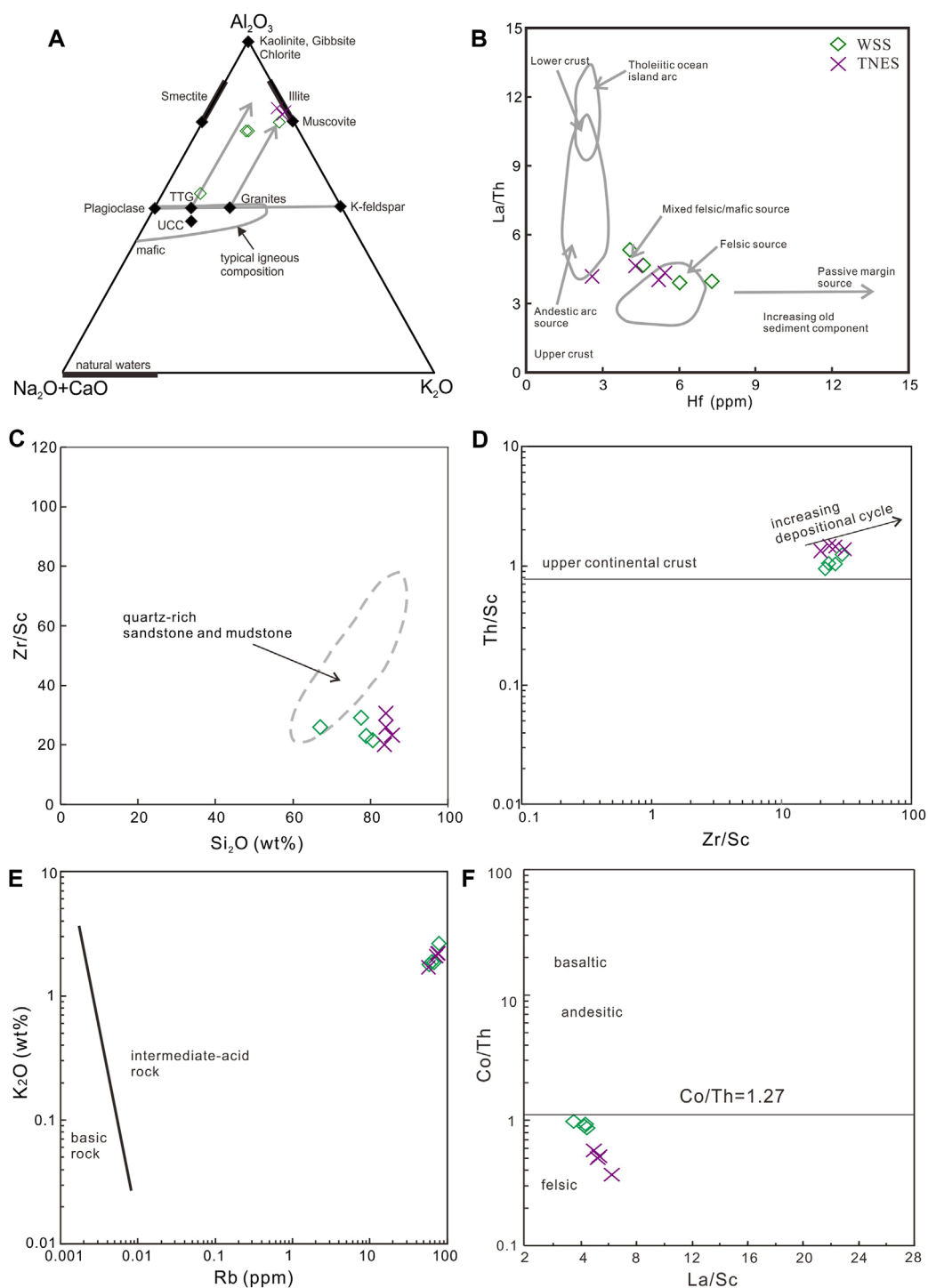Age vs Th/U diagrams of detrital zircons from the WSS and TNES.

FIGURE 9
Source rock discrimination diagrams for the studied sandstones and mudstones. **(A)** A−CN−K ternary plot for the studied sandstones and mudstones; **(B)** La/Th *versus* Hf diagram (after Floyd and Leveridge, 1987); **(C)** SiO₂vs Zr/Sc; **(D)** Zr/Sc vs Th/Sc (after Cingolani et al., 2003); **(E)** Rb vs K₂O (after Spalletti et al., 2008); **(F)** La/Sc vs Co/Th (after Gu et al., 2002)

instances of reverse order sedimentation have been observed in this upper part, along with widespread development of sheet sandstone, strongly indicative of a delta front facies. In the TNES, the upper part of the T_3x_2 does not exhibit marked differences from the middle-lower part and is believed to have been deposited in a braided delta front facies.

To accurately determine the depositional age of the T_3x_2, zircon U-Pb dating was conducted on two samples each from the WSS and the TNES. In sample WYG2 from the WSS, the youngest group of five zircons has an average age of 220.5 Ma. Conversely, sample WYG3 from the WSS contains a single youngest zircon with age of 275.6 Ma. Sample TJG1 from the TNES has a youngest grouping of

eight zircons with an average age of 240.0 Ma, while sample TJG3 has a youngest grouping of seven zircons with an average age of 240.7 Ma. The detrital zircon dating indicates that the youngest sediment in both the WSS and TNES is 220.5 Ma, suggesting the actual depositional period is subsequent to this age. Therefore, assigning a late Triassic age to the T_3x_2 appears reasonable. The TNES's more consistent and abundant late Triassic zircon crystals, compared to the WSS, could be attributed to the absence of the upper part in the WSS.

6.2 Source rock and provenance

6.2.1 Source rock features

The palaeo-weathering and source rock composition of clastic rocks can be traced using whole-rock geochemical indicators. The Chemical Index of Alteration (CIA, Nesbitt and Young, 1984), evaluates the ratio of stable minerals to clay minerals and is effective in assessing paleo-weathering conditions. Unweathered magmatic rocks typically exhibit CIA values around 40–50, whereas intense weathering can elevate these values to as high as 100 (Li et al., 2008; Fathy et al., 2023). In the WSS, three sandstone samples exhibit CIA values ranging from 73 to 75, with one sample showing a notably lower value of 54. In contrast, four sandstone samples from the TNES have uniform CIA values of 78–80, indicating a slightly higher degree of paleo-weathering compared to the WSS samples. Some layers in the WSS contain samples that are almost fresh, suggesting minimal weathering.

The increase of clay minerals such as kaolinite and illite, a sign of more intense weathering (Nesbitt and Young, 1984), is evident in the Al_2O_3–Na_2O + CaO–K_2O diagram (Figure 9A). Interestingly, one sandstone sample from the WSS deviates from the general trend, hinting that its weathering is mainly driven by plagioclase, unlike the other samples where illite plays a more significant role. The Al_2O_3–Na_2O + CaO parallel regression lines are useful in tracking the composition of source rocks (Nesbitt and Young, 1984; Li et al., 2008). In most of the examined samples, these lines intersect at a point between granites and tonalite–trondhjemite–granodiorite (TTG) on the plagioclase–K-feldspar line. This suggests that the primary source rocks are granites, TTG, and rocks with mixed signatures.

Trace elements are more effective in distinguishing source rocks than major elements due to their lower mobility during erosion, transportation, and diagenesis (Ryan and Williams, 2007). Samples from the WSS and TNES show low La/Th ratios and variable Hf contents, they plot in the field of felsic source and mixed felsic/mafic source, indicating an upper crustal affinity (Figure 9B). Additionally, these samples exhibit high La/Sc, Th/Cr, Th/Co, and Th/Sc ratios, aligning them with the compositional traits of upper continental crust and siliceous sandstones rather than lower continental crust, oceanic crust, or mafic sandstones. This indicates that their source rocks are predominantly upper crustal felsic materials. On various diagrams such as SiO_2–Zr/Sc, Zr/Sc–Th/Sc, Rb–K_2O, and La/Sc–Co/Th (Figure 9C–F), the samples consistently fall in the fields of quartz-rich sandstone and mudstone, upper crust with increasing depositional cycle, intermediate-acid rock and felsic rock, respectively. Consequently, it is deduced that the primary source rocks for these samples were mainly upper crustal felsic rocks.

This can also be proven in upper crust normalized diagrams because they show flat REE distribution patterns that are approximately 1, indicating the samples have REE concentrations very much similar to the average upper crust. Moreover, their upper crust normalized trace elements are also fluctuate near 1 except Sr and P, indicating they are originated from specific upper crust materials that are enriched in P and depleted in Sr.
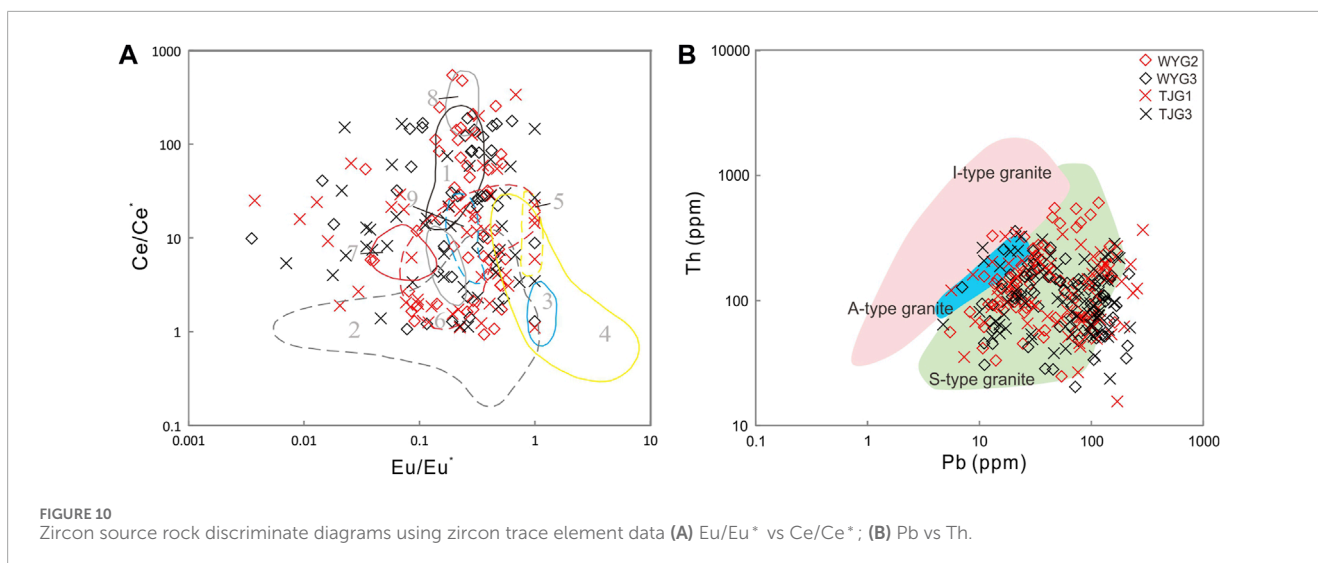
6.2.2 Source rock of detrital zircons

The analysis of trace elements in zircons is an effective tool for deducing the source or protolith of metamorphic and igneous rocks. The Th/U ratio is particularly useful in differentiating between metamorphic and magmatic zircons. Typically, zircons crystallized in magmas exhibit Th/U ratios above 0.4, while those influenced by metamorphic processes generally show ratios below 0.1 (Xiao et al., 2018; Li et al., 2021; Zhang et al., 2022). In samples WYG2 and WYG3, the bulk of detrital zircons have Th/U ratios over 0.3, with only a minority ranging between 0.1 and 0.3 or below 0.1. For samples TJG1 and TJG3, while most detrital zircons have Th/U ratios above 0.3, there is a notable fraction between 0.1 and 0.3, and a smaller subset below 0.1. This indicates that detrital zircons from the WSS are largely magmatic, with a small proportion undergoing slight or complete metamorphic alteration. In contrast, the TNES samples contain a large number of magmatic zircons and a significant proportion of zircons slightly altered (0.1<Th/U<0.3), with a smaller number fully metamorphosed. This reflects the higher degree of paleo-weathering observed in the TNES samples.

Trace elements in magmatic zircons are often employed to determine the nature of their host rocks, as zircons from various magma types display distinct elemental concentrations (Belousova et al., 2002; Zhang et al., 2023a; Xiao et al., 2023). By excluding all metamorphic zircons with Th/U ratios less than 0.3, the remaining zircons, which are magmatic in origin, can be used to deduce the characteristics of their host rocks using their trace elements content. Detrital magmatic zircons from the WSS generally exhibit Eu/Eu* ratios ranging from 0.1 to 1 and variable Ce/Ce* ratios, which mainly plot in an intermediate-acid rock field, suggesting felsic host rocks. In contrast, detrital magmatic zircons from the TNES show diverse Eu/Eu* and Ce/Ce* ratios, suggesting a greater inclusion of zircons from mafic rocks (Figure 10A). To more precisely trace their host rocks, Pb and Th contents in zircons were used to distinguish between A-, I-, and S-type granites. This is crucial as I-type granite magmas generally exhibit higher Th and lower Pb concentrations compared to S-type granites (Wang et al., 2012). The detrital zircons from the WSS and TNES, with their relatively high Pb contents exceeding 10 ppm, indicate that their host rocks are primarily S-type granites (Figure 10B).

6.2.3 Provenance

Detrital zircons extracted from the sandstone samples of the WSS and the TNES exhibit poor roundness, suggesting they have undergone only short transport distances. Analysis of two sandstone samples from each of these sections reveals similar age distributions, with shared age peaks at 220 Ma, 450 Ma, 800 Ma, and 1800 Ma, and a minor peak at 2,500 Ma. Zircons from the WSS show a predominant peak at 800 Ma and include a greater proportion of zircons that are younger than 500 Ma. In contrast, zircons from

FIGURE 10
Zircon source rock discriminate diagrams using zircon trace element data **(A)** Eu/Eu* vs Ce/Ce*; **(B)** Pb vs Th.

the TNES exhibit a main peak at 1800 Ma, suggesting that the provenance of the WSS is relatively younger compared to the TNES.

The Yangtze Block, when compared to adjacent blocks, exhibits a unique detrital zircon age spectrum with major peaks at 2,500 Ma, 1800 Ma, and 800 Ma (Figure 11). The oldest peak at 2,500 Ma is indicative of the early formation of the Yangtze Block's continental core (Guo et al., 2015). The 1850 Ma peak potentially signifies the Yangtze Block's integration into the formation of the global supercontinent Colombia (Yin et al., 2013). Meanwhile, the 800 Ma peak corresponds to the consolidation of the Yangtze and Cathaysia Blocks, an event traditionally dated to the period between 1,000–750 Ma, linked to the Jiangnan Orogeny (Yao et al., 2015). Although the main age peaks of the Yangtze Block at 2,500 Ma, 1850 Ma, and 800 Ma are similar to those in the WSS and the TNES, it is noteworthy that the Yangtze Block lacks the 450 Ma and 220 Ma peaks found in the WSS and TNES.

The Qinling Orogenic Belt exhibits complex detrital zircon age spectra. In the North Qinling Belt, the zircon age spectra reveal older peaks at 2,500 Ma, 900 Ma, and 750 Ma, along with younger peaks at 400 Ma and 200 Ma (Figure 11). In comparison, the South Qinling Belt shows age peaks at 2,500 Ma, 750 Ma, and 450 Ma (Figure 11). These differing age spectra between the North and South Qinling Belts reflect their different affinity before the Neoproterozoic. The North Qinling Belt, with a significant age peak at 2,500 Ma and several others between 1850–1,600 Ma, shares similarities with the North China Craton, suggesting its development from the south edge of this craton (Bai et al., 2021; Li et al., 2023b; Ying et al., 2024). The South Qinling Belt, with age peaks at 2,500 Ma, 750 Ma, and 450 Ma, and evidence of magmatic events around 1800 Ma, resembles the Yangtze Block, suggesting its origin from the northern edge of the Yangtze Block (Nie et al., 2016; Wang et al., 2020). When compared to the age spectra of the WSS and TNES, only the North Qinling Belt displays a peak at 900 Ma. Both the North and South Qinling Belts have peaks at 750 Ma, while only the North Qinling Belt exhibits a younger peak at 200 Ma.
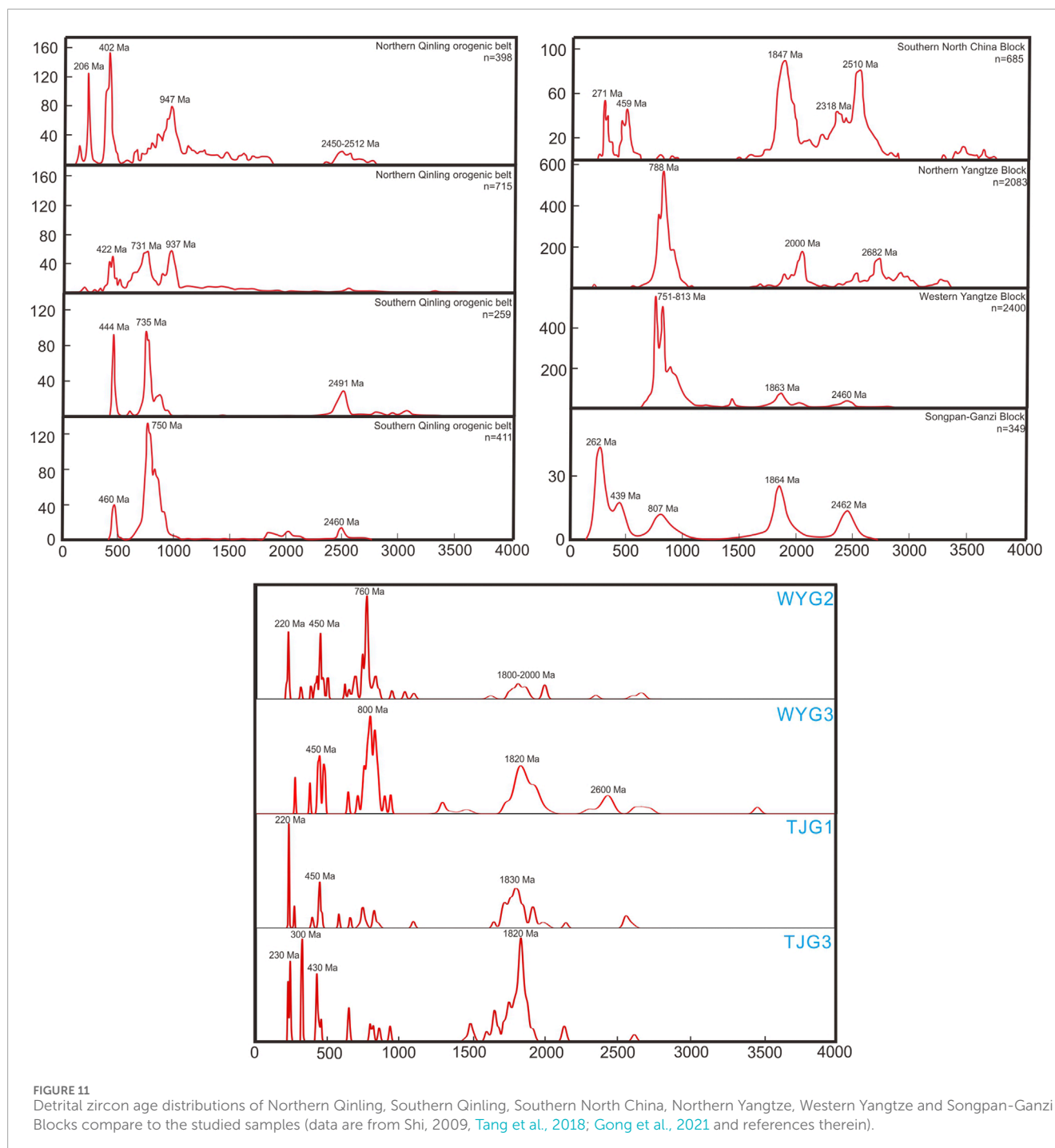
Detrital zircons from the Songpan-Ganzi Terrane display age spectra with major peaks at 2,500 Ma, 1850 Ma, 800 Ma, 450 Ma, and 300 Ma, closely mirroring the age spectra of the WSS and TNES

(Figure 11). Despite these similarities, numerous studies suggest that the Songpan-Ganzi Terrane is unlikely to be the provenance of the Xujiahe Formation for several reasons. Firstly, the Xujiahe Formation's lithic fragments predominantly comprise limestone, sandstone, and quartzite, distinctly different from the sediment types in the Songpan-Ganzi terrane and Longmenshan strike-slip fault zone (Tang et al., 2018). Secondly, the Hf isotope signatures of detrital zircons from the Xujiahe Formation closely match those from the Qinling orogenic belt, suggesting a direct affinity (Yu and Liang, 2017; Zhang et al., 2020). Finally, paleocurrent analyses show that the ancient rivers, which carried the detrital zircons to the study areas, flowed from the north or northeast towards the south or southwest (Gong et al., 2021), a pattern inconsistent with an origin in the Songpan-Ganzi Terrane and more indicative of the Qinling Orogenic Belt.

Overall, the Qinling Orogenic Belt is the most probable source for the sedimentary material found in the WSS and TNES. Paleogeographically, the depositional environment of the Xujiahe Formation was a braided delta located at the intersection angle between the Qinling Orogenic Belt and Yangtze Block. Previous studies have proposed the presence of an ancient river flowing from the north to the south, forming a littoral delta in the south along the Paleo-Tethys Ocean (Gong et al., 2021). Thus, it seems likely that the sediments of the WSS and TNES originated from the Qinling Orogenic Belt. However, a comparison of detrital zircon ages indicates that those from the North Qinling Orogenic Belt are more closely aligned with the WSS and TNES than the South Qinling. The WSS predominantly features zircons aged 750–800 Ma, implying a primary sediment source from the South Qinling but with some input from the North Qinling. Conversely, the TNES appears to have a larger proportion of sediments from the North Qinling, with a smaller contribution from the South Qinling.

6.3 Tectonic implications

Sandstone samples from both the WSS and the TNES display high quartz content and low proportions of feldspar and lithic

FIGURE 11
Detrital zircon age distributions of Northern Qinling, Southern Qinling, Southern North China, Northern Yangtze, Western Yangtze and Songpan-Ganzi Blocks compare to the studied samples (data are from Shi, 2009, Tang et al., 2018; Gong et al., 2021 and references therein).

fragments. The lithic fragments in these samples are largely sedimentary, with a moderate representation of magmatic fragments and the least contribution from metamorphic fragments. This composition, dominated by quartz and sedimentary fragments, indicates that the sandstones are composed of recycled crustal materials (Dickinson and Suczek, 1979; Dickinson et al., 1983). On the Qt-F-L and Qm-F-Lt diagrams, all samples fall within the recycled orogenic field, specifically under the quartzose recycled category, indicating an orogenic tectonic setting for the formation of these sandstones (Figures 12A,B). Furthermore, the geochemistry

of these sediments can also be used to trace their depositional tectonic setting (Bhatia, 1983; Bhatia and Crook, 1986). Based on the $K_2O/Na_2O–SiO_2/Al_2O_3$, $Fe_2O_3 + MgO–TiO_2$, $SiO_2–K_2O/Na_2O$, and $Fe_2O_3 + MgO–Al_2O_3/SiO_2$ diagrams, the TNES samples align with a passive margin setting. Whereas, the WSS samples span both passive and active continental margin settings, indicating a potential transitional tectonic setting from a passive to an active continental margin (Figure 12C–F).

Previous studies indicate that the study area was formed within a foreland basin environment during the Late Triassic (Luo et al.,
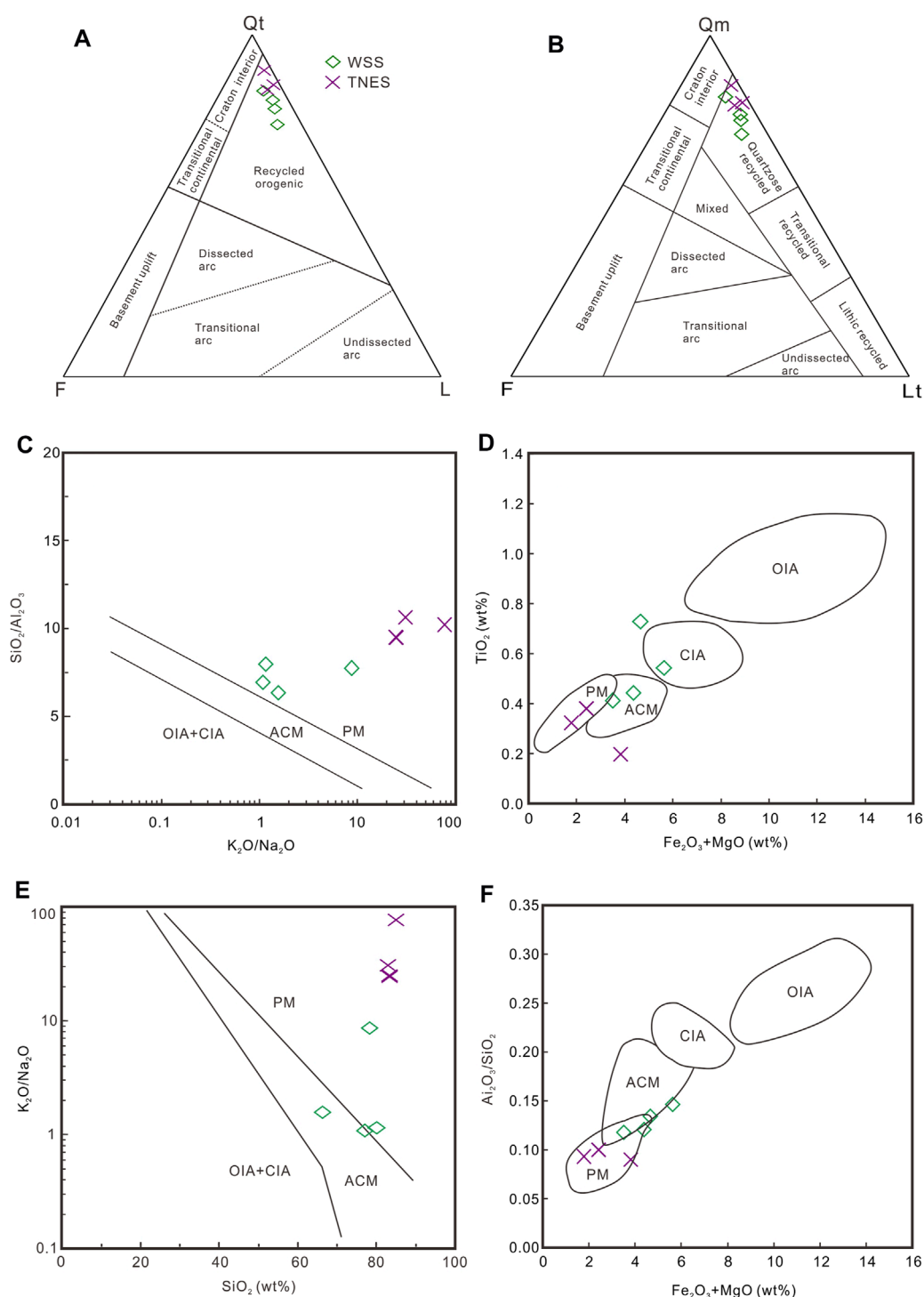
FIGURE 12
(A) Qt−F−L plot; **(B)** Qm−F−Lt plot. Parameters are from Dickinson and Suczek (1979), Dickinson et al. (1983) and Dickinson (1985); **(C)** K₂O/Na₂O vs SiO₂/Al₂O₃; **(D)** Fe₂O₃ + MgO vs TiO₂; **(E)** SiO₂ vs K₂O/Na₂O; **(F)** Fe₂O₃ + MgO vs Al₂O₃/SiO₂. Abbreviation: PM-passive margin, ACM-active continental margin, CIA-continental island arc, OIA-oceanic island arc.

2013; Li et al., 2014; Luo et al., 2019; Mu et al., 2019; Deng et al., 2022). The subduction of the Paleo-Tethys Oceanic lithosphere started northward in the Early Permian and shifted southward in the Early Triassic (Ding et al., 2013; Fathy et al., 2024). During the late Triassic, the Paleo-Tethys Ocean underwent a scissor-like closure

from east to west. While the eastern segments of the South China and North China Blocks were already joined along the Qinling and Dabie orogenic belts, the western part formed a gulf with multiple rivers and appendant delta. This remaining segment of the Paleo-Tethys Ocean was flanked by the Kunlun and western Qinling
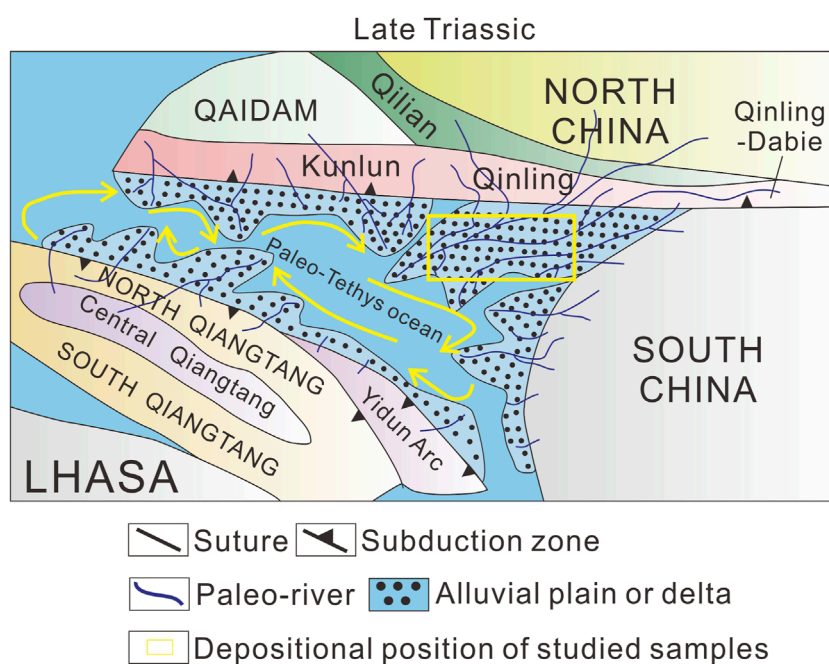
FIGURE 13
Provenance model of the T_3x_2 in late Triassic.

orogenic belts to the north, the South China Block to the east, and the Qiangtang Block to the south. The study area was located at the Northeastern corner of the gulf, and it was deposit under the condition of braided delta formed by several rivers oriented from northeast to southwest. These paleo rivers may originate from North China Block and South China Block, but they mainly flow through the Qinling orogenic belt (Figure 13). Hence, they brought abundant sediments to the study area and formed the super thick Xujiahe formation.

7 Conclusion

Sandstones in two sections (WSS and TNES) of the T_3x_2 were carried out for source rock and provenance study. The T_3x_2 sandstones were deposited during the Late Triassic in a braided delta facies, which exhibit moderate degrees of paleo-weathering, indicating that their source rocks were primarily upper crustal felsic rocks, predominantly S-type granites.

The sediment provenance of the T_3x_2 sandstones was mainly the Qinling Orogenic Belt. However, the WSS predominantly contains a majority of sediments originated from the South Qinling, while the TNES primarily contains a majority of sediments originated from the North Qinling.

The depositional environment of the T_3x_2 transitioned from a passive to an active continental margin setting. This change was concurrent with the east-to-west scissor-like closure of the Paleo-Tethys Ocean, resulting in the formation of a littoral braided delta shaped by multiple rivers flowing from the northeast to the southwest.

Data availability statement

The original contributions presented in the study are included in the article/Supplementary Material, further inquiries can be directed to the corresponding authors.

Author contributions

FX: Formal Analysis, Methodology, Resources, Writing–original draft. WX: Data curation, Formal Analysis, Investigation, Methodology, Supervision, Writing–review and editing. MS: Funding acquisition, Investigation, Methodology, Project administration, Writing–review and editing. IVS: Data curation, Funding acquisition, Investigation, Writing–review and editing. MSA: Data curation, Investigation, Resources, Writing–review and editing. CZ: Data curation, Investigation, Resources, Writing–review and editing. YW: Investigation, Resources, Writing–review and editing. BY: Investigation, Resources, Writing–review and editing. BH: Investigation, Validation, Writing–review and editing. NL: Investigation, Validation, Writing–review and editing. DF: Data curation, Investigation, Resources, Writing–review and editing.

Acknowledgments

Conflict of interest

The authors declare that the research was conducted in the absence of any commercial or financial relationships that could be construed as a potential conflict of interest.

Publisher's note

All claims expressed in this article are solely those of the authors and do not necessarily represent those of their affiliated organizations, or those of the publisher, the editors and the reviewers. Any product that may be evaluated in this article, or claim that may be made by its manufacturer, is not guaranteed or endorsed by the publisher.

Supplementary material

The Supplementary Material for this article can be found online at: https://www.frontiersin.org/articles/10.3389/feart.2024.1444679/full#supplementary-material

References

Bai, B., Chen, D., Zhu, X., Ren, Y., Luo, F., Wang, H., et al. (2021). ~1.77 Ga A-type granite and dark enclaves in the North qinling orogenic belt: constrains on the tectonic affinity between the North qinling orogenic belt and the North China craton. *Precambrian Res.* 357, 106117. doi:10.1016/j.precamres.2021.106117

Belousova, E., Griffin, W., O'Reilly, S. Y., and Fisher, N. (2002). Igneous zircon: trace element composition as an indicator of source rock type. *Contrib. Mineral. Petrol.* 143 (5), 602–622. doi:10.1007/s00410-002-0364-7

Bhatia, M. R. (1983). Plate tectonics and geochemical composition of sandstones. *J. Geol.* 91, 611–627. doi:10.1086/628815

Bhatia, M. R., and Crook, K. A. W. (1986). Trace element characteristics of graywackes and tectonic setting discrimination of sedimentary basins. *Contrib. Mineral. Petrol.* 92, 181–193. doi:10.1007/bf00375292

Cai, W., Xie, R., Li, H., Dou, S., Li, S., Deng, S., et al. (2024). Developmental characteristics of fractures in deep tight sandstone reservoirs in the second Member of the Xujiahe Formation of Zhongjiang Gas Field. *Unconv. Resour.* 100073. doi:10.1016/j.uncres.2024.100073

Charvest, J. (2013). The neoproterozoic–early paleozoic tectonic evolution of the South China block: an overview. *J. Asian Earth Sci.* 74, 198–209. doi:10.1016/j.jseaes.2013.02.015

Chen, G., Hu, F., Robertson, H. F. A., Garzanti, E., Zhang, S., and Wu, F. Y. (2023). A combined methodology for reconstructing source-to-sink basin evolution, exemplified by the Triassic Songpan–Ganzi basin, Central China. *Sediment. Geol.* 458, 106529. doi:10.1016/j.sedgeo.2023.106529

Cingolani, C. A., Manassero, M., and Abre, P. (2003). Composition, provenance and tectonic setting of Ordovician siliciclastic rocks in the San Rafael block: southern extension of the Precordillera crustal fragment, Argentina. *J. S. Am. Earth Sci.* 16 (1), 91–106. doi:10.1016/s0895-9811(03)00021-x

Deng, J., Liu, M., Ji, Y., Tang, D., Zeng, Q., Song, L., et al. (2022). Controlling factors of tight sandstone gas accumulation and enrichment in the slope zone of foreland basins: the Upper Triassic Xujiahe Formation in Western Sichuan Foreland Basin, China. *J. Pet. Sci. Eng.* 214, 110474. doi:10.1016/j.petrol.2022.110474

Dickinson, W. R. (1985). "Interpreting provenance relations from detrital modes of sandstones," in *Provenance of arenites*. Editor G. G. Zuffa (NATO ASI Series), 148, 333–361. doi:10.1007/978-94-017-2809-6_15

Dickinson, W. R., Beard, L. S., Brakenridge, G. R., Erjavec, J. L., Ferguson, R. C., Inman, K. F., et al. (1983). Provenance of North American Phanerozoic sandstones in relation to tectonic setting. *Geol. Soc. Am. Bull.* 94, 222–235. doi:10.1130/0016-7606(1983)94<222:ponaps>2.0.co;2

Dickinson, W. R., and Suczek, C. A. (1979). Plate tectonics and sandstone compositions. *Am. Assoc. Pet. Geol. Bull.* 63, 2164–2182. doi:10.1306/2f9188fb-16ce-11d7-8645000102c1865d

Ding, L., Yang, D., Cai, F. L., Pullen, A., Kapp, P., Gehrels, G. E., et al. (2013). Provenance analysis of the Mesozoic Hoh-XilSongpan- Ganziturbidites in northern Tibet: implications for the tectonic evolution of the eastern paleo-Tethys ocean. *Tectonics* 32, 34–48. doi:10.1002/tect.20013

Fathy, D., Abart, R., Wagreich, M., Gier, S., Ahmed, M. S., and Sami, M. (2023). Late campanian climatic-continental weathering assessment and its influence on source rocks deposition in southern Tethys, Egypt. *Minerals* 13 (2), 160. doi:10.3390/min13020160

Fathy, D., Baniasad, A., Littke, R., and Sami, M. (2024). Tracing the geochemical imprints of Maastrichtian black shales in southern Tethys, Egypt: assessing hydrocarbon source potential and environmental signatures. *Int. J. Coal Geol.* 283, 104457. doi:10.1016/j.coal.2024.104457

Floyd, P. A., and Leveridge, B. E. (1987). Tectonic environment of the Devonian Gramscatho basin, south Cornwall: framework mode and geochemical evidence from turbiditic sandstones. *J. Geol. Soc.* 144, 531–542. doi:10.1144/gsjgs.144.4.0531

Gong, D. X., Wu, C. H., Zou, H., Zhou, X., Zhou, Y., Tan, H. Q., et al. (2021). Provenance analysis of late Triassic turbidites in the eastern Songpan-Ganzi flysch complex: sedimentary record of tectonic evolution of the eastern Paleo-Tethys ocean. *Mar. Pet. Geol.* 126 (1), 104927. doi:10.1016/j.marpetgeo.2021.104927

Gou, L., Lu, G., Deng, B., Wang, C., Li, Z., Yu, Y., et al. (2024). Tectonic–paleogeographic evolution of the Late Triassic in the Sichuan basin, SW China: constraints from sedimentary facies and provenance analysis of the Xujiahe Formation. *Mar. Pet. Geol.* 160, 106649. doi:10.1016/j.marpetgeo.2023.106649

Gu, X. X., Liu, J. M., Zheng, M. H., Tang, J. X., and Qi, L. (2002). Provenance and tectonic setting of the Proterozoic turbidites in Hunan, south China: geochemical evidence. *J. Sediment. Res.* 72 (3), 393–407. doi:10.1306/081601720393

Guo, L. J., Wu, Y. B., Gao, S., Jin, Z. M., Zong, K. Q., Hu, Z. C., et al. (2015). Episodic paleoarchean-paleoproterozoic (3.3-2.0 Ga) granitoid magmatism in Yangtze craton, South China: implications for late archean tectonics. *Precambrian Res.* 270, 246–266. doi:10.1016/j.precamres.2015.09.007

Han, B. N., Jiang, Y. H., Liu, Y. C., and Ni, C. Y. (2024). Middle to Late Triassic felsic and mafic magmatism in the eastern West Qinling Orogen, Central China: a record of the Paleo-Tethyan oceanic crust advance to retreat. *Lithos* 464-465, 107451. doi:10.1016/j.lithos.2023.107451

Hao, L., Yang, D., Wang, A., Quan, Y., Yan, X., and Wang, S. (2024). Petrogenesis of early Paleozoic granitoids in the North Qinling Orogen, Central China: implications

for crustal evolution in an accretionary orogen. *Geosci. Front.* 15 (2), 101764. doi:10.1016/j.gsf.2023.101764

Herron, M. M. (1988). Geochemical classification of terrigenous sands and shales from core or log data. *J. Sediment. Petrol.* 58, 820–829. doi:10.1306/212f8e77-2b24-11d7-8648000102c1865d

Hu, Z., Liu, Y., Chen, L., Zhou, L., Li, M., Zong, K., et al. (2011). Contrasting matrix induced elemental fractionation IN NIST SRM and rock glasses during laser ablation ICP-MS analysis at high spatial resolution. *J. Anal. At. Spectrom.* 26 (2), 425–430. doi:10.1039/c0ja00145g

Huang, Y., Liu, Z., Li, P., Liu, J., Liao, C., and Xu, S. (2020). Analysis of lithofacies and evaluation of effective reservoirs of member 2 of Xujiahe Formation in the Xinchang area in Western Sichuan. *Pet. Res.* 5 (3), 244–253. doi:10.1016/j.ptlrs.2020.08.002

Ingersoll, R. V., Bullard, T. F., Ford, R. L., Grimm, J. P., and Sares, S. W. (1984). The effect of grain size on detrital modes: a test of the gazzi-dickinson point-counting method (holocene, sand, New Mexico, USA). *J. Sediment. Petrol.* 54 (1), 103–116. doi:10.1306/212F83B9-2B24-11D7-8648000102C1865D

Jiang, Z., Ran, B., Li, Z., Liu, S., Wang, Z., Han, Y., et al. (2023). A late triassic depositional age for the Xujiahe formation, Sichuan Basin: implications for the closure of the Paleo-Tethys Ocean. *Mar. Pet. Geol.* 155, 106346. doi:10.1016/j.marpetgeo.2023.106346

Li, M., Zhang, Y., Huang, C., O, J., Hinnov, L., Wan, Y., et al. (2017). Astronomical tuning and magnetostratigraphy of the upper triassic xujiahe formation of south China and newark supergroup of north America: implications for the late triassic time scale. *Earth Planet. Sci. Lett.* 475 (1), 207–223. doi:10.1016/j.epsl.2017.07.015

Li, Q. G., Liu, S. W., Wang, Z. Q., Chu, Z. Y., Song, B., Wang, Y. B., et al. (2008). Contrasting provenance of Late Archean metasedimentary rocks from the Wutai Complex, North China Craton: detrital zircon U-Pb, whole-rock Sm-Nd isotopic, and geochemical data. *Int. J. Earth Sci.* 97, 443–458. doi:10.1007/s00531-007-0170-6

Li, S. L., Lai, J. Q., Xiao, W. Z., Belousova, E. A., Rushmer, T., Zhang, L. J., et al. (2021). Crustal growth event in the Cathaysia Block at 2.5 Ga: evidence from chronology and geochemistry of captured zircons in Jurassic acidic dykes. *Geol. Mag.* 158, 567–582. doi:10.1017/s0016756820000667

Li, Y., Shao, L., Eriksson, K. A., Tong, X., Gao, C., and Chen, Z. (2014). Linked sequence stratigraphy and tectonics in the Sichuan continental foreland basin, upper triassic xujiahe formation, southwest China. *J. Asian Earth Sci.* 88, 116–136. doi:10.1016/j.jseaes.2014.02.025

Li, Z., Lei, X., Han, Z., Qiao, Q., and Yan, J. (2023a). Geomorphic characteristics of the tongbai-dabie mountain area and their indicative significance. *J. Xinyang Norm. Univ. Nat. Sci. Ed.* 36 (4), 523–527. (In Chinese with English abstract). doi:10.3969/j.issn.1003-0972.2023.04.002

Li, Z., Ma, X., An, W., Mitchell, R. N., Li, Q., Lan, Z., et al. (2023b). Provenance transition of the mesoproterozoic–neoproterozoic xuhuai basin: constraining the accretion of the Northern qinling terrane with the North China craton. *J. Asian Earth Sci.* 251, 105675. doi:10.1016/j.jseaes.2023.105675

Liao, T., Hu, J., Zhang, F., and Liu, L. (2010). Reconsideration of the sediment characteristics of the second member of the triassic Xujiahe Formation in sanhuaiba, huaying mountain. *Min. Sci. Technol. (China)* 20 (4), 591–599. doi:10.1016/s1674-5264(09)60250-7

Liu, J., Liu, Z., Liu, Z., Liu, Y., Shen, B., Xiao, K., et al. (2023). Geological characteristics and models of fault-fold-fracture body in deep tight sandstone of the second member of Upper Triassic Xujiahe Formation in Xinchang structural belt of Sichuan Basin, SW China. *Pet. Explor. Dev.* 50 (3), 603–614. doi:10.1016/s1876-3804(23)60413-6

Liu, J., Liu, Z., Xiao, K., Huang, Y., and Jin, W. (2020). Characterization of favorable lithofacies in tight sandstone reservoirs and its significance for gas exploration and exploitation: a case study of the 2nd Member of Triassic Xujiahe Formation in the Xinchang area, Sichuan Basin. *Pet. Explor. Dev.* 47 (6), 1194–1205. doi:10.1016/s1876-3804(20)60129-5

Liu, Y., Gao, S., Hu, Z., Gao, C., Zong, K., and Wang, D. (2010a). Continental and oceanic crust recycling-induced melt-peridotite interactions in the trans-North China orogen: U-Pb dating, Hf isotopes and trace elements in zircons from mantle xenoliths. *J. Petrol.* 51 (51), 537–571. doi:10.1093/petrology/egp082

Liu, Y. S., Hu, Z. C., Zong, K. Q., Gao, C. G., Gao, S., Xu, J., et al. (2010b). Reappraisal and refinement of zircon U-Pb isotope and trace element analyses by LA-ICP-MS. *Sci. Bull.* 55 (15), 1535–1546. doi:10.1007/s11434-010-3052-4

Ludwig, K. R. (2003). *User's manual for isoplot 3.00: a geochronological toolkit for microsoft excel.* Berkeley: Berkeley Geochronology Center, Special Publication. no. 4.

Luo, L., Meng, W., Gluyas, J., Tan, X., Gao, X., Feng, M., et al. (2019). Diagenetic characteristics, evolution, controlling factors of diagenetic system and their impacts on reservoir quality in tight deltaic sandstones: typical example from the Xujiahe Formation in Western Sichuan Foreland Basin, SW China. *Mar. Pet. Geol.* 103, 231–254. doi:10.1016/j.marpetgeo.2019.02.012

Luo, L., Qi, J. F., Zhang, M. Z., Wang, K., and Han, Y. Z. (2013). Detrital zircon U–Pb ages of Late–Jurassic deposits in the western and northern Sichuan Basin margin: constrains on the foreland basin provenance and tectonic implications. *Int. J. Earth Sci.* 103, 553–1568. doi:10.1007/s00531-014-1032-7

Mu, H., Yan, D. P., Qiu, L., Yang, W. X., Kong, R. Y., Gong, L. X., et al. (2019). Formation of the late triassic western sichuan foreland basin of the qinling orogenic belt, SW China: sedimentary and geochronological constraints from the xujiahe Formation. *J. Asian earth Sci.* 183, 103938. doi:10.1016/j.jseaes.2019.103938

Nesbitt, H. W., and Young, G. M. (1984). Prediction of some weathering trends of plutonic and volcanic rocks based on thermodynamic and kinetic considerations. *Geochim. Cosmochim. Acta* 48, 1523–1534. doi:10.1016/0016-7037(84)90408-3

Nie, H., Yao, J., Wan, X., Zhu, X. Y., Siebel, W., and Chen, F. (2016). Precambrian tectonothermal evolution of South Qinling and its affinity to the Yangtze Block: evidence from zircon ages and Hf-Nd isotopic compositions of basement rocks. *Precambrian Res.* 286, 167–179. doi:10.1016/j.precamres.2016.10.005

Pettijohn, F. J., Potter, P. E., and Siever, R. (1972). *Sand and sandstone.* New York: Springer.

Pullen, A., Kapp, P., Gehrels, G. E., Vervort, J. D., and Ding, L. (2008). Triassic continental subduction in central Tibet and MediTerranean-style closure of the paleo-Tethys ocean. *Geology* 36 (5), 351–354. doi:10.1130/g24435a.1

Qiu, L., Yan, D. P., Yang, W. X., Wang, J., Tang, X., and Ariser, S. (2017). Early to middle triassic sedimentary records in the youjiang basin, South China: implications for indosinian orogenesis. *J. Asian Earth Sci.* 141 (15), 125–139. doi:10.1016/j.jseaes.2016.09.020

Qiu, X. F., Ling, W. L., Liu, X. M., Lu, S. S., Jiang, T., Wei, Y. X., et al. (2018). Evolution of the Archean continental crust in the nucleus of the Yangtze block: evidence from geochemistry of 3.0 Ga TTG gneisses in the Kongling high-grade metamorphic Terrane, South China. *J. Asia Earth Sci.* 154, 149–161. doi:10.1016/j.jseaes.2017.12.026

Ryan, K. M., and Williams, D. M. (2007). Testing the reliability of discrimination diagrams for determining the tectonic depositional environment of ancient sedimentary basins. *Chem. Geol.* 242, 103–125. doi:10.1016/j.chemgeo.2007.03.013

She, Z. B. (2007). *Detrital zircon geochronology of the upper Proterozoic-Mesozoic clastic rocks in the mid-upper Yangtze region.* Wuhan: China University of Geoscience Phd. Thesis, 1–143. (In Chinese with English abstract).

Spalletti, L. A., Queralt, I., Matheos, S. D., Colombo, F., and Maggi, J. (2008). Sedimentary petrology and geochemistry of siliciclastic rocks from the upper Jurassic Tordillo Formation (Neuquén Basin, western Argentina): implications for provenance and tectonic setting. *J. S. Am. Earth Sci.* 25 (4), 440–463. doi:10.1016/j.jsames.2007.08.005

Sun, S. S., and McDonough, W. F. (1989). "Chemical and isotopic systematics of oceanic basalts: implications for mantle composition and processes,". *Magmatism in the ocean basins.* Editors A. D. Saunders, and M. J. Norry (Geological Society, London, Special Publications), 42, 313–345. doi:10.1144/gsl.sp.1989.042.01.19

Tang, X., Yang, W., Yan, Y., Guo, Y., Zhang, Y., and Yang, L. (2023). Characteristics of trace elements in pyrite and their implications for the genesis of yindongpo gold deposit in henan Province. *J. Xinyang Norm. Univ. Nat. Sci. Ed.* 36 (3), 445–450. (In Chinese with English abstract). doi:10.3969/j.issn.1003-0972.2023.03.017

Tang, Y., Zhang, Y., and Tong, L. (2018). Mesozoic-Cenozoic evolution of the Zoige depression in the Songpan-Ganzi flysch basin, eastern Tibetan plateau: constraints from detrital zircon U-Pb ages and fission-track ages of the Triassic sedimentary sequence. *J. Asian Earth Sci.* 151, 285–300. doi:10.1016/j.jseaes.2017.10.021

Taylor, S. R., and McLennan, S. M. (1985). *The continental crust: its composition and evolution.* Oxford: Blackwell.

Wang, H., Wu, W., Liu, S., Zhang, X., Song, J., Li, S., et al. (2020). Initial separation of the South qinling terrane from the Yangtze block during the ediacaran: insights from sequence correlation and zircon Hf isotope of tuff. *Mar. Pet. Geol.* 122, 104613. doi:10.1016/j.marpetgeo.2020.104613

Wang, Q., Zhu, D. C., Zhao, Z. D., Guan, Q., Zhang, X. Q., Sui, Q. L., et al. (2012). Magmatic zircons from I-S- and A-type granitoids in Tibet: trace element characteristics and their application to detrital zircon provenance study. *J. Asian Earth Sci.* 53, 59–66. doi:10.1016/j.jseaes.2011.07.027

Xiao, W., Lai, J., Jeffrey, M., Mao, X., Chen, Y., Ou, Q., et al. (2018). Tectonic affinity and evolution of the Alxa Block during the Neoproterozoic: constraints from zircon U-Pb dating, trace elements, and Hf isotopic composition. *Geol. J.* 54 (6), 3700–3719. doi:10.1002/gj.3343

Xiao, W., Liu, C., Tan, K., Duan, X., Shi, K., Sui, Q., et al. (2023). Two distinct fractional crystallization mechanisms of A-type granites in the nanling range, South China: a case study of the Jiuyishan complex massif and xianghualing intrusive stocks. *Minerals* 13 (5), 605. doi:10.3390/min13050605

Xu, X. (2023). Late triassic to middle Jurassic tectonic evolution of the South China block: geodynamic transition from the paleo-tethys to the paleo-pacific regimes. *Earth-Science Rev.* 241, 104404. doi:10.1016/j.earscirev.2023.104404

Yan, D. P., Qiu, L., Wells, M. L., Zhou, M. F., Meng, X., Lu, S., et al. (2018a). Structural and geochronological constraints on the early mesozoic north longmen Shan thrust belt: foreland fold-thrust propagation of the SW qinling orogenic belt, northeastern Tibetan plateau. *Tectonics* 37 (12), 4595–4624. doi:10.1029/2018tc004986

Yan, D. P., Zhou, Y., Qiu, L., Wells, M. L., Mu, H., and Xu, C. G. (2018b). The Longmenshan Tectonic Complex and adjacent tectonic units in the eastern

margin of the Tibetan Plateau: a review. *J. Asian Earth Sci.* 164 (15), 33–57. doi:10.1016/j.jseaes.2018.06.017

Yang, P., Zhang, L., Liu, K., Cao, B., Gao, J., and Qiu, G. (2021). Diagenetic history and reservoir evolution of tight sandstones in the second member of the Upper Triassic Xujiahe Formation, western Sichuan Basin, China. *J. Pet. Sci. Eng.* 201, 108451. doi:10.1016/j.petrol.2021.108451

Yang, R. C., Li, C. J., Fan, A. P., Zong, M., and Zhang, T. (2013). Research progress and development trend of provenance analysis of terrigenous sedimentary rock. *J. Sediment.* 31, 99–107. (In Chinese with English abstract). doi:10.14027/j.cnki.cjxb.2013.01.018

Yao, J., Shu, L., Santosh, M., and Li, J. (2015). Neoproterozoic arc-Related andesite and orogeny-related unconformity in the eastern Jiangnan orogenic belt: constraints on the assembly of the Yangtze and Cathaysia blocks in South China. *Precambrian Res.* 262, 84–100. doi:10.1016/j.precamres.2015.02.021

Yin, C., Lin, S., Davis, S. W., Zhao, G., Xiao, W., Li, L., et al. (2013). 2.1-1.85Ga tectonic events in the Yangtze Block, South China: petrological and geochronological evidence from the Kongling Complex and implications for the reconstruction of supercontinent Columbia. *Lithos* 182-183, 200–210. doi:10.1016/j.lithos.2013.10.012

Ying, Y. C., Chen, W., Wu, Y. B., and Jiang, S. Y. (2024). Microtexture, geochemistry and geochronology of monazite and zircon from the Jialu deposit in the Lesser Qinling: implications for multi-stage magmatic and metamorphic events in the southern margin of the North China Craton. *J. Asian Earth Sci.* 260, 105971. doi:10.1016/j.jseaes.2023.105971

Yu, S. H., and Liang, X. Q. (2017). Provenance of the xujiahe group of late triassic in the westren Sichuan Basin: evidence from detrital zircon U-Pb ages. *Sci. Technol. Eng.* 17 (4), 13–24. (In Chinese with English abstract). doi:10.3969/j.issn.1671-1815.2017.04.002

Yuan, D., Tang, X., Shi, X., Bao, J., Liu, K., Fan, J., et al. (2022). Zircon geochronology and geochemistry of the taohualing pluton in northern dabieshan and their tectonic implications. *J. Xinyang Norm. Univ. Nat. Sci. Ed.* 35 (1), 97–102. (In Chinese with English abstract). doi:10.3969/j.issn.1003-0972.2022.01.016

Zhang, C., Li, C., Jiang, J., Qin, H., Liu, M., Zhou, H., et al. (2022). Geochemical characteristics of REE and trace elements compositions and geological significance of longhuo gold-antimony deposit in guangxi. *J. Xinyang Norm. Univ. Nat. Sci. Ed.* 35 (1), 103–107. (In Chinese with English abstract). doi:10.3969/j.issn.1003-0972.2022.01.017

Zhang, C., Liu, D., Liu, Q., Jiang, S., Wang, X., Wang, Y., et al. (2023b). Magmatism and hydrocarbon accumulation in sedimentary basins: a review. *Earth-Science Rev.* 244, 104531. doi:10.1016/j.earscirev.2023.104531

Zhang, C., Liu, D., Zhang, X., Spencer, C., Kong, X., Zeng, J., et al. (2020). Hafnium isotopic disequilibrium during sediment melting and assimilations. *Geochem. Perspect.* 12, 34–39. doi:10.7185/geochemlet.2001

Zhang, C., Liu, Y., Yao, Y., Yan, Y., and Shi, X. (2023a). Characteristics of mineralogy and its implications for ore-forming mechanism of the apalieke Cu-polymetallic deposit in xinjiang. *J. Xinyang Norm. Univ. Nat. Sci. Ed.* 36 (1), 76–81. (In Chinese with English abstract). doi:10.3969/j.issn.1003-0972.2023.01.012

Zhang, L., Zhang, R., Wu, K., Chen, Y., Li, C., Hu, Y., et al. (2018). Late Cretaceous granitic magmatism and mineralization in the Yingwuling W–Sn deposit, South China: constraints from zircon and cassiterite U–Pb geochronology and whole-rock geochemistry. *Ore Geol. Rev.* 96, 115–129. doi:10.1016/j.oregeorev.2018.04.012

Zhang, L. Y., Ding, L., Pullen, A., Xu, Q., Liu, D. L., Cai, F. L., et al. (2014). Age and geochemistry of western hoh-xil–songpan-ganzi granitoids, northern tibet: implications for the mesozoic closure of the Paleo-Tethys Ocean. *Lithos* 190-191, 328–348. doi:10.1016/j.lithos.2013.12.019

Zhang, S. B., and Zheng, Y. F. (2013). Formation and evolution of Precambrian continental lithosphere in South China. *Gondwana Res.* 23, 1241–1260. doi:10.1016/j.gr.2012.09.005

Zhou, G., Wei, G., and Hu, G. (2019). The geochemical and organic petrological characteristics of coal measures of the xujiahe formation in the sichuan basin, China. *Energy explor. Exploit.* 37 (3), 889–906. doi:10.1177/0144598719842332